Journal of Computational Physics 229 (2010) 8105–8129

Contents lists available at ScienceDirect

Journal of Computational Physics

journal homepage: www.elsevier.com/locate/jcp

Hybrid weighted essentially non-oscillatory schemes with different indicators ☆

Gang Li [a,b], Jianxian Qiu [a,*]

[a] Department of Mathematics, Nanjing University, Nanjing, Jiangsu 210093, PR China
[b] School of Mathematical Science, Qingdao University, Qingdao, Shandong 266071, PR China

ARTICLE INFO

Article history:
Received 19 May 2010
Received in revised form 9 July 2010
Accepted 9 July 2010
Available online 18 July 2010

Keywords:
WENO approximation
Up-wind linear approximation
Troubled-cell indicator
Hyperbolic conservation laws
Hybrid schemes

ABSTRACT

A key idea in finite difference weighted essentially non-oscillatory (WENO) schemes is a combination of lower order fluxes to obtain a higher order approximation. The choice of the weight to each candidate stencil, which is a nonlinear function of the grid values, is crucial to the success of WENO schemes. For the system case, WENO schemes are based on local characteristic decompositions and flux splitting to avoid spurious oscillation. But the cost of computation of nonlinear weights and local characteristic decompositions is very high. In this paper, we investigate hybrid schemes of WENO schemes with high order up-wind linear schemes using different discontinuity indicators and explore the possibility in avoiding the local characteristic decompositions and the nonlinear weights for part of the procedure, hence reducing the cost but still maintaining non-oscillatory properties for problems with strong shocks. The idea is to identify discontinuity by an discontinuity indicator, then reconstruct numerical flux by WENO approximation in discontinuous regions and up-wind linear approximation in smooth regions. These indicators are mainly based on the troubled-cell indicators for discontinuous Galerkin (DG) method which are listed in the paper by Qiu and Shu (J. Qiu, C.-W. Shu, A comparison of troubled-cell indicators for Runge–Kutta discontinuous Galerkin methods using weighted essentially non-oscillatory limiters, SIAM Journal of Scientific Computing 27 (2005) 995–1013). The emphasis of the paper is on comparison of the performance of hybrid scheme using different indicators, with an objective of obtaining efficient and reliable indicators to obtain better performance of hybrid scheme to save computational cost. Detail numerical studies in one- and two-dimensional cases are performed, addressing the issues of efficiency (less CPU time and more accurate numerical solution), non-oscillatory property.

1. Introduction

In this paper, we systematically investigate hybrid schemes of WENO schemes with high order up-wind linear schemes using different discontinuity indicators for hyperbolic conservation laws:

$$\begin{cases} u_t + \nabla \cdot f(u) = 0, \\ u(x,0) = u_0(x). \end{cases} \tag{1.1}$$

These indicators are mainly based on the troubled-cell indicators for discontinuous Galerkin methods which are listed by Qiu and Shu [18]. The emphasis is on the comparisons of performances of the hybrid WENO schemes using different

☆ The research was partially supported by NSFC Grant No. 10931004.
* Corresponding author. Tel.: +86 25 8359 6053; fax: +86 25 8359 7130.
E-mail addresses: gangli1978@163.com (G. Li), jxqiu@nju.edu.cn (J. Qiu).

0021-9991/$ - see front matter © 2010 Elsevier Inc. All rights reserved.
doi:10.1016/j.jcp.2010.07.012

indicators, with an objective of obtaining efficient and reliable indicators to get better performance for the hybrid WENO schemes to save computational cost.

The first WENO scheme is constructed by Liu et al. [16] for a third-order finite volume version, in which they adopted a convex combination of the reconstructions on all candidate stencils instead of choosing the smoothest stencil to pick one interpolating polynomial for the essentially non-oscillatory (ENO) schemes [11], while additionally obtaining one order of improvement in accuracy. In 1996, the third and fifth-order finite difference WENO schemes in multi space dimensions are constructed by Jiang and Shu [14], with a general framework for the design of smoothness indicators and nonlinear weights. Balsara and Shu [2] extended the WENO schemes up to the eleventh order, and Gerolymos et al. [10] further developed and investigated very high-order WENO schemes up to the seventeenth order. WENO schemes are the important high-resolution/high-order methods for the numerical solutions of hyperbolic conservation laws. WENO schemes have been quite successful in applications, especially for problems containing both shocks and complicated smooth solution structures, such as compressible turbulence simulations [13,17,25] and aeroacoustics [8]. For more details, we refer to lecture notes [22,23] and the references listed therein.

A key idea in finite difference WENO schemes is a combination of lower order fluxes to obtain a higher order approximation. The choice of the weight to each candidate stencil, which is a nonlinear function of the grid values, is crucial to the success of WENO schemes. For the system case, WENO schemes are based on local characteristic decompositions and flux splitting to avoid spurious oscillation. But the cost of computation of nonlinear weights and local characteristic decompositions is very high. There have been a lot of efforts in the literature in order to overcome this drawback. For Euler equations, Jiang and Shu [14] computed the nonlinear weights from pressure and entropy instead of the characteristic values to simplify the costly characteristic decomposition procedure. Pirozzoli [17] developed an efficient hybrid compact-WENO scheme, which relied on a compact up-wind scheme in conservative form to treat smooth regions of the flow field and on a WENO scheme to handle discontinuities. Hill and Pullin [13] developed a hybrid scheme combining the tuned center-difference scheme with a WENO scheme which is then constructed for use in the large-eddy simulations of strongly compressible, shock-driven flows. They expected that the nonlinear weights for WENO schemes would be achieved automatically in regions of smooth flow away from shocks to match those of the tuned center-difference scheme, but in practice a switch was found to be necessary. Costa et al. [9] proposed a high-order hybrid central-WENO finite difference scheme. They used high order multi-resolution analysis of Harten [12] to detect the high gradient parts of the solution in order to capture the shocks with the fifth-order WENO scheme, while the smooth regions are computed with the more efficient and accurate sixth-order central finite difference scheme. The efforts above attempted mainly to hybridize the WENO scheme and other schemes. The main idea is to use the WENO scheme to capture discontinuities and to use other efficient schemes in smooth regions of the solution to save the computational cost.

An important component of the hybrid scheme is an indicator to automatically identify where the discontinuity of the solution is and the expensive WENO approximation is applied in the discontinuous regions, and an efficient approximation is applied in the other regions. In this paper, we investigate hybrid schemes of WENO schemes with high order up-wind linear schemes using different discontinuity indicators and explore the possibility in avoiding the local characteristic decompositions and the nonlinear weights for part of the procedure, hence reducing the cost but still maintaining non-oscillatory properties for problems with strong shocks. The idea is to identify discontinuity by an discontinuity indicator, then to reconstruct numerical flux by WENO approximation in discontinuous regions and by up-wind linear approximation in smooth regions. These indicators are mainly based on the troubled-cell indicators for DG methods, also call limiter, which are listed by Qiu and Shu [18] . For example, the minmod-based TVB limiter [6,5,4,7] is a slope limiter using a technique borrowed from the finite volume methodology; the moment-based limiter [1] and an improved moment limiter [3] are designed specifically for DG method. Recently, a limiter [15] based on a strong superconvergence at the outflow boundary of each element in smooth regions for the DG method was designed to detect discontinuities for hyperbolic systems of conservation laws. There are also many other limiters in the finite volume and finite difference literature, such as the monotonicity-preserving (MP) limiter [24], and modifications of MP limiter [19]. Qiu and Shu compared the performances of the limiters above as troubled-cell indicators for Runge–Kutta discontinuous Galerkin (RKDG) methods using WENO limiters in [18]. Recently, Zhu and Qiu used these limiters as troubled-cell indicators for adaptive RKDG methods in [28].

The emphasis of the paper is on comparison of the performance of hybrid scheme using different indicators, with an objective of obtaining efficient and reliable indicators to obtain better performance of hybrid scheme to save computational cost. The organization of this paper is as follows: In Section 2, we review the procedure of hybrid WENO schemes with high order up-wind linear schemes and present description of troubled-cell indicators. Detailed numerical studies in one- and two-dimensional cases are performed, addressing the issues of efficiency (less CPU time and more accurate numerical solution), non-oscillatory property in Section 3, and concluding remarks are given in Section 4.

2. Description of hybrid WENO schemes with high order up-wind linear schemes

In this section we give the details of the procedure of hybrid schemes of WENO schemes with high order up-wind linear schemes. We start with the description in the one-dimensional case. We consider the one-dimensional scalar conservation laws:

$$\begin{cases} u_t + f(u)_x = 0, \\ u(x,0) = u_0(x). \end{cases} \tag{2.1}$$

For simplicity, we assume that the grid points $\{x_j\}$ are uniform with $x_{j+1} - x_j = \Delta x$, $x_{j+1/2} = x_j + \Delta x/2$ and denote the cells by $I_j = [x_{j-1/2}, x_{j+1/2}]$. A semidiscrete conservative high-order finite difference scheme of (2.1) is

$$\frac{du_j(t)}{dt} = -\frac{1}{\Delta x}\left(\hat{f}_{j+1/2} - \hat{f}_{j-1/2}\right), \tag{2.2}$$

where $u_j(t)$ is the numerical approximation to the point value $u(x_j,t)$, and the numerical flux $\hat{f}_{j+1/2}$ approximates $h_{j+1/2} = h(x_{j+1/2})$ to a high-order accuracy with $h(x)$ implicitly defined as in [14]:

$$f(u(x)) = \frac{1}{\Delta x}\int_{x-\Delta x/2}^{x+\Delta x/2} h(\xi)d\xi. \tag{2.3}$$

To take up-winding into account, we split a general flux into two parts either globally or locally:

$$f(u) = f^+(u) + f^-(u), \tag{2.4}$$

where $df^+(u)/du \geqslant 0$ and $df^-(u)/du \leqslant 0$. For simplicity, we define:

$$f^+(u) = \frac{1}{2}(f(u) + \alpha u), \quad f^-(u) = \frac{1}{2}(f(u) - \alpha u), \tag{2.5}$$

where $\alpha = \max_u|f'(u)|$ and the maximum is taken over the whole relevant range of u. This is the global Lax–Friedrichs flux splitting. The numerical fluxes $\hat{f}^+_{j+1/2}$ and $\hat{f}^-_{j+1/2}$ are relative to $f^+(u)$ and $f^-(u)$, respectively and will be reconstructed by either WENO approximation in the discontinuous regions or high order up-wind linear approximation in the smooth regions. The detail of reconstruction of numerical fluxes $\hat{f}_{j+1/2}$ will be presented in Section 2.2. Then we have the numerical flux:

$$\hat{f}_{j+1/2} = \hat{f}^+_{j+1/2} + \hat{f}^-_{j+1/2},$$

and the semidiscrete scheme (2.2), written as an ordinary differential equation (ODE) system:

$$u_t = L(u)$$

is then discretized in time by a total variation diminishing (TVD) Runge–Kutta method [20,21], for example the third order version given by

$$\begin{aligned} u^{(1)} &= u^n + \Delta t L(u^n) \\ u^{(2)} &= \frac{3}{4}u^n + \frac{1}{4}u^{(1)} + \frac{1}{4}\Delta t L\left(u^{(1)}\right) \\ u^{n+1} &= \frac{1}{3}u^n + \frac{2}{3}u^{(2)} + \frac{2}{3}\Delta t L\left(u^{(2)}\right). \end{aligned} \tag{2.6}$$

An important component of the hybrid scheme is to automatically identify where the discontinuity of the solution is and high WENO reconstruction is applied in the discontinuous regions, and efficient reconstruction is applied in the smooth regions. We will use the troubled-cell indicators borrowed from DG methods in [18] to identify the troubled cells, namely the cells where the discontinuity of the solution is, the description of different troubled-cell indicators will be presented in Section 2.3.

2.1. Algorithm of hybrid WENO scheme

The procedure of hybrid $2r+1$ order WENO schemes with $2r+1$ order up-wind linear schemes is then described in the following:

Step 1. The troubled-cell indicator is applied to identify troubled cell, namely the locations of discontinuity of the numerical solution, only once at the beginning of the Runge–Kutta time discretization procedure.

Step 2. Reconstruction of the numerical flux based on either the $2r+1$ order WENO approximation in the discontinuous regions or the $2r+1$ order up-wind linear approximation in the smooth regions. The numerical fluxes $\hat{f}^+_{j+1/2}$ and $\hat{f}^-_{j-1/2}$ will be reconstructed by WENO approximations in the stencils which contain a troubled cell identified in the Step 1. For example, let I_{j_0} to be a troubled cell, then there are $2r+1$ stencils $\{x_{j_0-r+l},\ldots,x_{j_0+r+l}\}, l=-r,\cdots,r$ which contain a discontinuity, the numerical fluxes $\hat{f}^+_{j_0+l+1/2}$ and $\hat{f}^-_{j_0+l-1/2}, l=-r,\cdots,r$ will be reconstructed by $2r+1$ order WENO approximation in these stencils. And the numerical fluxes $\hat{f}^+_{j+l+1/2}$ and $\hat{f}^-_{j+l-1/2}$ will be reconstructed by $2r+1$ order up-wind linear approximation in the stencils which do not contain any troubled cells. Finally, we obtain the numerical fluxes in (2.2) $\hat{f}_{j+1/2} = \hat{f}^+_{j+1/2} + \hat{f}^-_{j+1/2}$, in which $\hat{f}^+_{j+1/2}, \hat{f}^-_{j+1/2}$ are reconstructed by WENO approximation or up-wind linear approximation.

2.2. The procedure for the reconstruction of numerical flux

In this subsection, we present the procedure for the reconstruction of numerical flux $\hat{f}^+_{j+1/2}$ by WENO approximation and high order up-wind linear approximation. The basic idea of the WENO approximation is to use a nonlinear convex combination of low-order polynomial interpolation approximations in order to yield a higher order approximation in smooth regions and use the idea of adaptive stencils to automatically achieve high-order accuracy and non-oscillatory property near discontinuities.

For the WENO approximation, $\hat{f}^+_{j+1/2}$ is expressed as [14]

$$\hat{f}^+_{j+1/2} = \sum_{k=0}^{r} \omega_k q^r_k(f^+_{j+k-r}, \ldots, f^+_{j+k}), \tag{2.7}$$

where ω_k is the nonlinear weight, $f^+_i = f^+(u_i), i = j-r, \ldots, j+r$, and

$$q^r_k(g_0, \ldots, g_r) = \sum_{l=0}^{r} a^r_{k,l} g_l \tag{2.8}$$

are the low-order approximation to $\hat{f}^+_{j+1/2}$ on the kth stencil $S_k = (x_{j+k-r}, \ldots, x_{j+k}), k = 0,1,\ldots,r$, and $a^r_{k,l}, 0 \leqslant k, l \leqslant r$, are constant coefficients, see [22] for details.

The nonlinear weight ω_k in (2.7) satisfies

$$\omega_k \geqslant 0, \quad \sum_{k=0}^{r} \omega_k = 1,$$

and is designed to yield $(2r+1)$ th-order accuracy in smooth regions of the solution. In [14,22] the nonlinear weight ω_k is formulated as

$$\omega_k = \frac{\alpha_k}{\sum_{l=0}^{r} \alpha_l}, \quad \text{with} \quad \alpha_k = \frac{C^r_k}{(\varepsilon + IS_k)^2}, \quad k = 0, 1, \ldots, r, \tag{2.9}$$

where C^r_k is the linear weight, for $r = 1,\ldots,4$, see Table 2.1. IS_k is a smoothness indicator of $f^+(u)$ on stencil S_k, $k = 0, 1,\ldots,r$, and ε is a small constant used here to avoid the denominator becoming zero, we take $\varepsilon = 10^{-6}$ in all test cases in this paper. We employed the smoothness indicators proposed in [14,22], i.e.,

$$IS_k = \sum_{l=1}^{r} \int_{x_{j-1/2}}^{x_{j+1/2}} (\Delta x)^{2l-1} (q^{(l)}_k)^2 dx,$$

where $q^{(l)}_k$ is the lth-derivative of $q_k(x)$ and $q_k(x)$ is the reconstruction polynomial of $f^+(u)$ on stencil S_k such that

$$\frac{1}{\Delta x} \int_{I_i} q_k(x) dx = f^+_i, \quad i = j+k-r, \ldots, j+k.$$

For the high order up-wind linear approximation, we use all the r candidate stencils, i.e., $S = \bigcup_{k=0}^{r} S_k$, which contains all $(2r+1)$ grid point values of $f^+(u)$, to obtain a $2r+1$ order approximation to $\hat{f}^+_{j+1/2}$ in smooth regions such that:

$$\frac{1}{\Delta x} \int_{I_i} q^{2r+1}_r(x) dx = f^+_i, \quad i = j-r, \ldots, j+r,$$

and

$$\hat{f}^+_{j+1/2} = q^{2r+1}_r\left(f^+_{j-r}, \ldots, f^+_{j+r}\right) = \sum_{l=0}^{2r} b_l f^+_{j+l-r}, \tag{2.10}$$

where $b_l, 0 \leqslant l \leqslant 2r$ are constant coefficients, for details, we refer to [22]. By simple algebra operation, we get:

$$\hat{f}^+_{j+1/2} = q^{2r+1}_r\left(f^+_{j-r}, \ldots, f^+_{j+r}\right) = \sum_{k=0}^{r} C^r_k q^r_k\left(f^+_{j+k-r}, \ldots, f^+_{j+k}\right), \tag{2.11}$$

Table 2.1
Optimal weights C^r_k.

C^r_k	$k=0$	$k=1$	$k=2$	$k=3$	$k=4$
$r=1$	1/3	2/3			
$r=2$	1/10	6/10	3/10		
$r=3$	1/35	12/35	18/35	4/35	
$r=4$	1/126	20/126	60/126	40/126	5/126

where the coefficient C_k^r here is the linear weight in (2.9), and in smooth regions $\omega_k = C_k^r + O((\Delta x)^r), k = 0, 1, \ldots, r$. Thus C_k^r bear the name of *optimal weights*.

The procedure for the reconstruction of $\hat{f}^-_{j+\frac{1}{2}}$ is a mirror symmetry to that of $\hat{f}^+_{j+1/2}$ with respect to $x_{j+1/2}$, we will not present it here to save space.

Remark 1. For the system cases, in order to achieve better qualities at the price of more complicated computations, the WENO approximation is always used with a local characteristic field decomposition, see e.g. [22] for details, while the upwind linear approximation is used component by component. For two-dimensional cases, the reconstruction of fluxes is based on dimension by dimension.

2.3. Description of the troubled-cell indicators

In this subsection we review a few troubled-cell indicators which mainly are based on DG method [18,28] to identify discontinuity of the numerical solution. And troubled-cell indicators based on the variation of the solution and multi-resolution analysis are also presented.

For convenience of presentation of the troubled-cell indicators, we construct a quadratic polynomial on cell I_j at time step t_n, denoted by $P_2(x)$:

$$P_2(x) = u_j^{(0)} + u_j^{(1)}\frac{x - x_j}{\Delta x} + u_j^{(2)}\left[\left(\frac{x - x_j}{\Delta x}\right)^2 - \frac{1}{12}\right], x \in \left[x_{j-1/2},\ x_{j+1/2}\right],$$

such that:

$$P_2(x_k) = u_k^n, \quad k = j-1, \quad j, j+1,$$

we have:

$$u_j^{(0)} = \frac{1}{24}\left(u_{j-1}^n + 22u_j^n + u_{j+1}^n\right), \quad u_j^{(1)} = \frac{1}{2}\left(u_{j+1}^n - u_{j-1}^n\right), \quad u_j^{(2)} = \frac{1}{2}\left(u_{j-1}^n - 2u_j^n + u_{j+1}^n\right).$$

Now we describe different troubled-cell indicators in detail:

1. Troubled-cell indicator based on the average total variation of the solution. (ATV, we will use the same abbreviation as in [18,28] for each indicator). Let TV denote the total variation of the solution at time step t_n,

$$TV \equiv TV(u^n) = \sum_j \left|u_{j+1}^n - u_j^n\right|.$$

If $|u_{j+1}^n - u_j^n| \geqslant \theta\frac{TV}{N}$, we declare that in cell $[x_j, x_{j+1}]$ the solution has a discontinuity, and cells I_j and I_{j+1} are identified as troubled cells. Here N is the number of cells. $0 < \theta < 1$ a constant, is the ATV parameter. The choice of θ depends on the solution. It is common in the literature to look at the variation of the solution in order to indicate the presence of discontinuities at a particular location [17,9]. Moreover this simple definition of the discontinuity guarantees that both shock waves and contact discontinuities are properly identified. But it is difficult to choose θ accurately, for θ is problem-dependent. If θ is chosen too small, this will increase computational cost unnecessarily; however if θ is chosen too large, spurious oscillations will appear.

2. The minmod-based TVB limiter [6] (TVB). Let:

$$\tilde{u}_j = P_2\left(x_{j+1/2}\right) - u_j^{(0)}, \quad \tilde{\tilde{u}}_j = -P_2\left(x_{j-1/2}\right) + u_j^{(0)}.$$

These are modified by the modified minmod function:

$$\begin{aligned} \tilde{u}_j^{(\mathrm{mod})} &= \tilde{m}\left(\tilde{u}_j, u_{j+1}^{(0)} - u_j^{(0)}, u_j^{(0)} - u_{j-1}^{(0)}\right), \\ \tilde{\tilde{u}}_j^{(\mathrm{mod})} &= \tilde{m}\left(\tilde{\tilde{u}}_j, u_{j+1}^{(0)} - u_j^{(0)}, u_j^{(0)} - u_{j-1}^{(0)}\right), \end{aligned} \tag{2.12}$$

where $\tilde{m}$ is given by

$$\tilde{m}(a_1, a_2, \ldots, a_n) = \begin{cases} a_1 & \text{if } |a_1| \leqslant M(\Delta x)^2, \\ m(a_1, a_2, \ldots, a_n) & \text{otherwise}, \end{cases} \tag{2.13}$$

and the minmod function m is given by

$$m(a_1, a_2, \ldots, a_n) = \begin{cases} s \cdot \min\limits_{1 \leqslant j \leqslant n} |a_j| & \text{if } \operatorname{sign}(a_1) = \operatorname{sign}(a_2) = \cdots = \operatorname{sign}(a_n) = s, \\ 0 & \text{otherwise}. \end{cases} \tag{2.14}$$

The TVB limiter parameter $M > 0$ is a constant.
If $\tilde{u}_j^{(\mathrm{mod})} \neq \tilde{u}_j$ or $\tilde{\tilde{u}}_j^{(\mathrm{mod})} \neq \tilde{\tilde{u}}_j$, we declare the cell I_j as a troubled cell.

Unfortunately, the TVB limiter parameter M is also dependent on the problem. There is no automatic switch which works well for various situations. For scalar problems it is possible to estimate M by the initial condition as in [6] (M is proportional to the second derivative of the initial data at smooth extrema), however it is difficulty to estimate M for system of equations. If M is chosen too small, more cells containing discontinuities will be identified than necessary, therefore increasing computational cost; however if M is chosen too large, spurious oscillations will appear.

3. The strong troubled-cell indicator of Xu and Shu [27] (XS). We define φ_j as

$$\varphi_j = \frac{\beta_j}{\beta_j + \gamma_j},$$

where

$$\alpha_j = (u_j^n - u_{j-1}^n)^2 + \varepsilon, \quad \beta_j = \left(\frac{\alpha_j}{\alpha_{j-1}} + \frac{\alpha_{j+1}}{\alpha_{j+2}}\right)^2, \quad \gamma_j = \frac{(u_{\max} - u_{\min})^2}{\alpha_j},$$

here ε is a positive constant which is introduced to avoid the denominator becoming zero (we will take $\varepsilon = 10^{-6}$ here). $u_{\max}, u_{\min}$ are maximum and minimum values of u_j^n for all grid points at time step t_n. It is clear that $0 \leqslant \varphi_i \leqslant 1$ and $\varphi_i = O(\Delta x^2)$ in smooth regions. When near a strong discontinuity, $\gamma_j \ll \beta_j$, φ_j is close to 1. In this paper, we identify the cells I_j and I_{j+1} as troubled cells when $\varphi_j > (\Delta x)^2$.

4. The monotonicity-preserving limiter [24] (MP). We define:

$$\text{median}(x, y, z) = x + m(y - x, z - x), \tag{2.15}$$

where m is the minmod function in (2.14). If:

$$u_{j+\frac{1}{2}}^- \neq \text{median}\left(u_{j+\frac{1}{2}}^-, u_{j+\frac{1}{2}}^{\min}, u_{j+\frac{1}{2}}^{\max}\right), \tag{2.16}$$

where

$$u_{j+\frac{1}{2}}^{\min} = \max\left[\min\left(u_j^{(0)}, u_{j+1}^{(0)}, u_{j+\frac{1}{2}}^{MD}\right), \quad \min\left(u_j^{(0)}, u_{j+\frac{1}{2}}^{UL}, u_{j+\frac{1}{2}}^{LC}\right)\right],$$
$$u_{j+\frac{1}{2}}^{\max} = \min\left[\max\left(u_j^{(0)}, u_{j+1}^{(0)}, u_{j+\frac{1}{2}}^{MD}\right), \quad \max\left(u_j^{(0)}, u_{j+\frac{1}{2}}^{UL}, u_{j+\frac{1}{2}}^{LC}\right)\right],$$

and

$$d_j = u_{j+1}^{(0)} - 2u_j^{(0)} + u_{j-1}^{(0)},$$
$$d_{j+\frac{1}{2}}^{M4X} = m\left(4d_j - d_{j+1}, 4d_{j+1} - d_j, d_j, d_{j+1}, d_{j-1}, d_{j+2}\right),$$
$$u_{j+\frac{1}{2}}^{MD} = \frac{1}{2}\left(u_j^{(0)} + u_{j+1}^{(0)} - d_{j+\frac{1}{2}}^{M4X}\right), \quad u_{j+\frac{1}{2}}^{UL} = u_j^{(0)} + \alpha\left(u_j^{(0)} - u_{j-1}^{(0)}\right),$$
$$u_{j+\frac{1}{2}}^{LC} = u_j^{(0)} + \frac{1}{2}\left(u_j^{(0)} - u_{j-1}^{(0)}\right) + \frac{\beta}{3}d_{j-\frac{1}{2}}^{M4X},$$

or if $u_{j-\frac{1}{2}}^+$ satisfies a similar (symmetric) condition, the cell I_j is identified as a troubled cell. We take the parameters $\alpha = 2$ and $\beta = 4$ as suggested in [24] in the numerical tests.

5. Multi-resolution analysis of Harten [12] (MR). Given the point values $\{u_j\}_0^N$ of function $u(x)$. Let $\tilde{u}_j$ denote the approximation to u_j which is obtained from the unique polynomial $\tilde{u}(x)$ of degree one that interpolates $u(x)$ at x_{j-1}, x_{j+1},

$$\tilde{u}_j = \tilde{u}(x_j) = \frac{1}{2}(u_{j-1} + u_{j+1}),$$

and let d_j denote the corresponding approximation error:

$$d_j = u_j - \tilde{u}_j.$$

If $u(x)$ at $x = \bar{x}$ has $p - 1$ continuous derivatives and a jump discontinuity in its p-th derivative as denoted by $[\cdot]$, then for x_j near $\bar{x}$:

$$d_j \approx \begin{cases} (\Delta x)^p [u^{(p)}], & p \leqslant 2, \\ (\Delta x)^2 u^{(2)}, & p \geqslant 2. \end{cases} \tag{2.17}$$

In this paper, if $|d_j| \geqslant \varepsilon_{MR}\Delta x$, the cell I_j is identified as a troubled cell, here ε_{MR} is a multi-resolution parameter.

6. Moment limiter of Biswas, Devine, and Flaherty [1] (BDF).

$$u_j^{(l),\text{mod}} = \frac{1}{(2l-1)} m\left((2l-1)u_j^{(l)}, \quad u_{j+1}^{(l-1)} - u_j^{(l-1)}, \quad u_j^{(l-1)} - u_{j-1}^{(l-1)}\right), \quad l = 1, 2, \tag{2.18}$$

where m is again the minmod function in (2.14). For our purpose, if the BDF limiter (2.18) returns other than the first argument for the highest order case $l = 2$, the cell I_j is identified as a troubled cell.

7. A modification of the moment limiter by Burbeau et al. [3] (BSB). If both (2.18) and

$$\hat{u}_j^{(l),\mathrm{mod}} = \frac{1}{(2l-1)} m\Big((2l-1)u_j^{(l)}, u_{j+\frac{1}{2}}^{(l-1)+} - u_j^{(l-1)}, u_j^{(l-1)} - u_{j-\frac{1}{2}}^{(l-1)-}\Big), \quad l = 1, 2, \tag{2.19}$$

where

$$u_{j+\frac{1}{2}}^{(l-1)+} = u_{j+1}^{(l-1)} - (2l-1)u_{j+1}^{(l)}, \quad u_{j-\frac{1}{2}}^{(l-1)-} = u_{j-1}^{(l-1)} + (2l-1)u_{j-1}^{(l)},$$

are enacted for the highest order moment $u_j^{(2)}$, then the cell I_j is identified as a troubled cell.

8. A modification of the MP limiter [19] (MMP). We let:

$$\phi = \min(1, \Delta\bar{u}^{\min}/\Delta_{\min}u), \tag{2.20}$$

where

$$\Delta\bar{u}^{\min} = u_j^{(0)} - \min\left(u_{j-1}^{(0)}, u_j^{(0)}, u_{j+1}^{(0)}\right), \quad \Delta_{\min}u = u_j^{(0)} - \min\left(u_{j-\frac{1}{2}}^{+}, u_{j+\frac{1}{2}}^{-}\right).$$

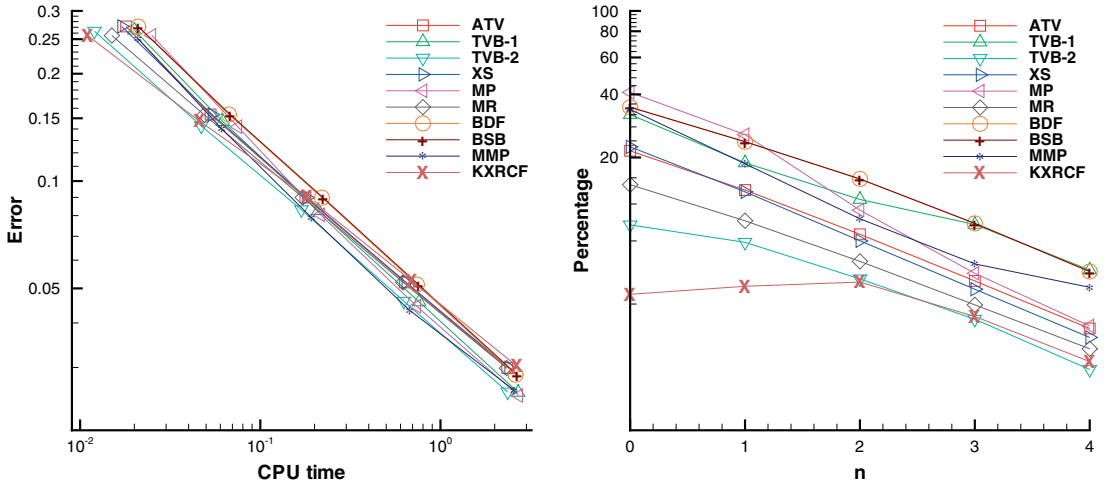

Fig. 3.1. Lax problem by the 3rd-order scheme. CPU-L_1-error (left) and cell-percentage (right).

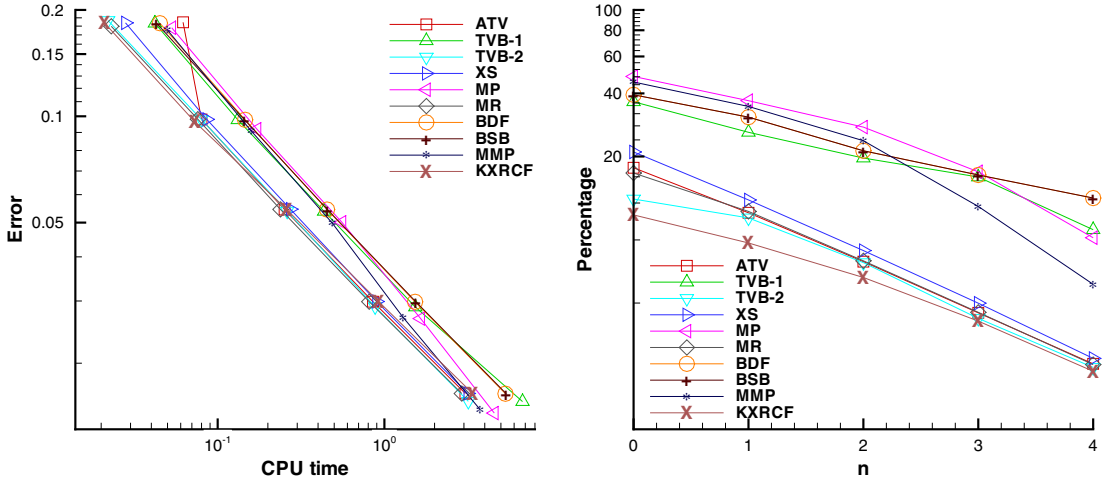

Fig. 3.2. Lax problem by the 5th-order scheme. CPU-L_1-error (left) and cell-percentage (right).

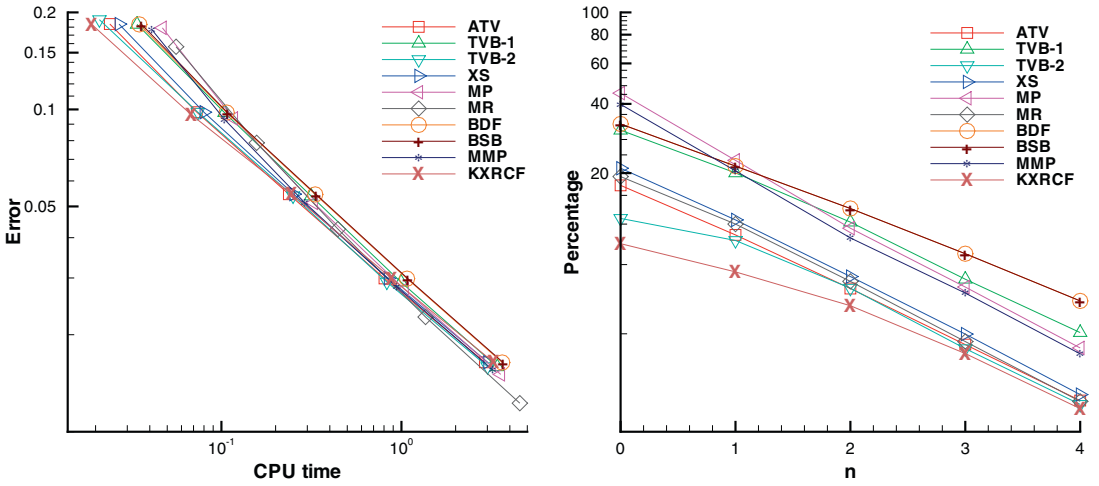

Fig. 3.3. Lax problem by the 7th-order scheme. CPU-L_1-error (left) and cell-percentage (right).

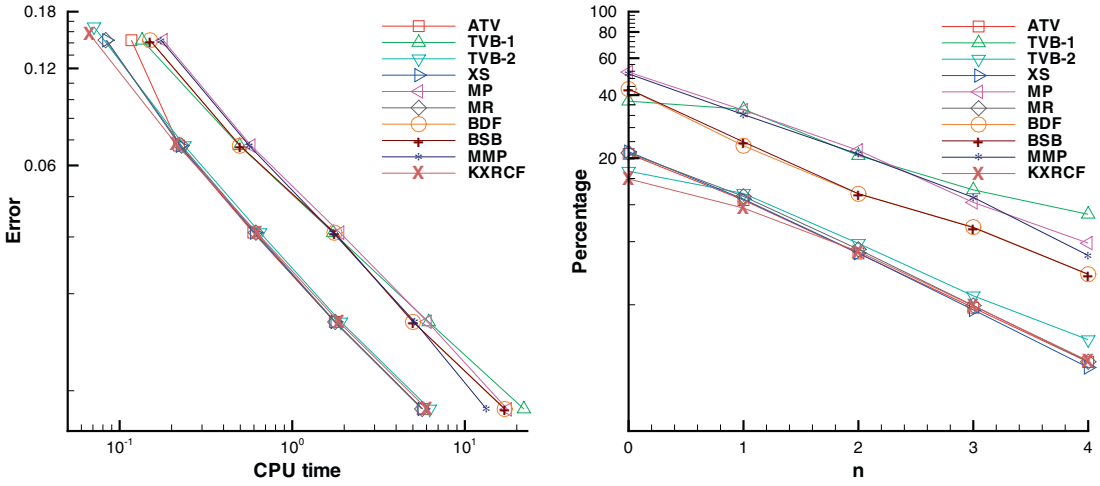

Fig. 3.4. Lax problem by the 9th-order scheme. CPU-L_1-error (left) and cell-percentage (right).

Table 3.2
Lax problem. The total CPU time of $N = 100 \times 2^n$ ($n = 0,1,\ldots,4$) cells, and the ratios of the total CPU time by the 3rd, 5th, 7th and 9th-order hybrid WENO schemes over that of the same order pure WENO scheme.

Scheme or indicators	Third-order scheme		Fifth-order scheme		Seventh-order scheme		Ninth-order scheme	
	CPU	Ratio	CPU	Ratio	CPU	Ratio	CPU	Ratio
WENO	14.61648	1.00	28.02074	1.00	73.82454	1.00	109.61222	1.00
ATV	3.30550	0.23	4.09538	0.15	6.452025	0.09	8.29474	0.08
TVB-1	5.35019	0.37	8.23175	0.29	22.19463	0.30	30.50436	0.28
TVB-2	3.26950	0.22	4.15637	0.15	6.99494	0.09	9.09462	0.08
XS	3.37549	0.23	4.19936	0.15	6.73500	0.09	8.31474	0.08
MP	4.50732	0.31	6.55900	0.23	16.07656	0.21	26.33300	0.24
MR	3.19452	0.22	4.04021	0.14	6.26320	0.08	8.00743	0.07
BDF	4.96425	0.33	6.98994	0.25	17.93128	0.24	24.42929	0.22
BSB	5.00424	0.34	7.10492	0.25	17.92528	0.24	24.49628	0.22
MMP	4.00739	0.27	5.35819	0.19	12.82105	0.17	20.95981	0.19
KXRCF	3.66244	0.25	4.43233	0.16	6.89395	0.09	8.79466	0.08

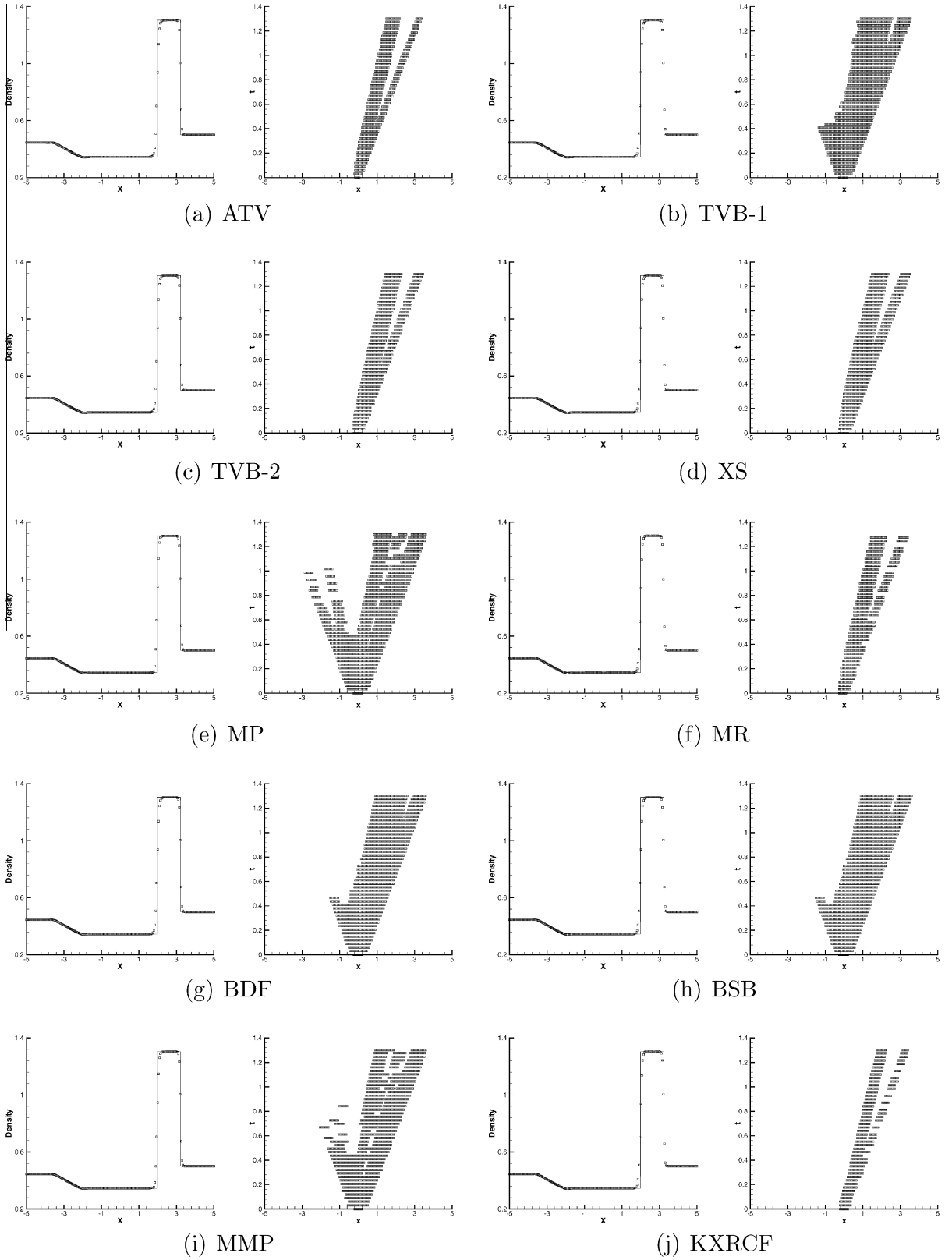

Fig. 3.5. Lax problem by the 5th-order scheme with different indicators, 200 cells, $t = 1.3$. Density and time history of reconstruction of fluxes by WENO approximation.

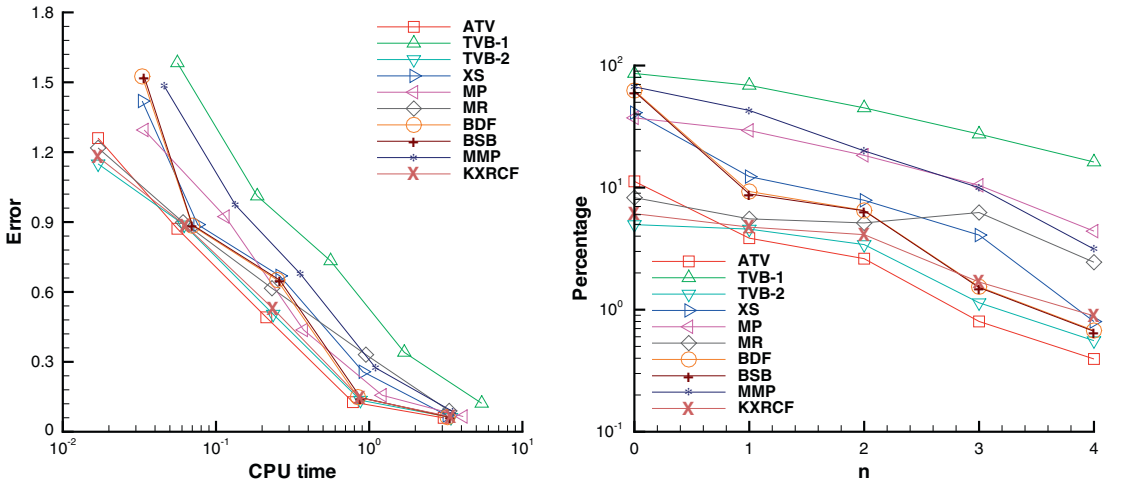

Fig. 3.6. The shock density wave interaction problem by the 3rd-order scheme. CPU-L_1-error (left) and cell-percentage (right).

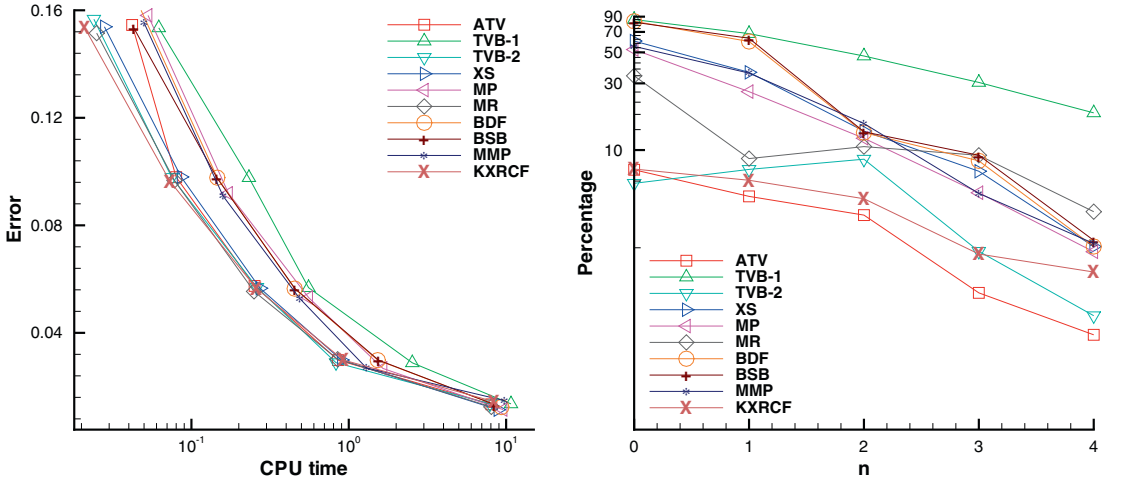

Fig. 3.7. The shock density wave interaction problem by the 5th-order scheme. CPU-L_1-error (left) and cell-percentage (right).

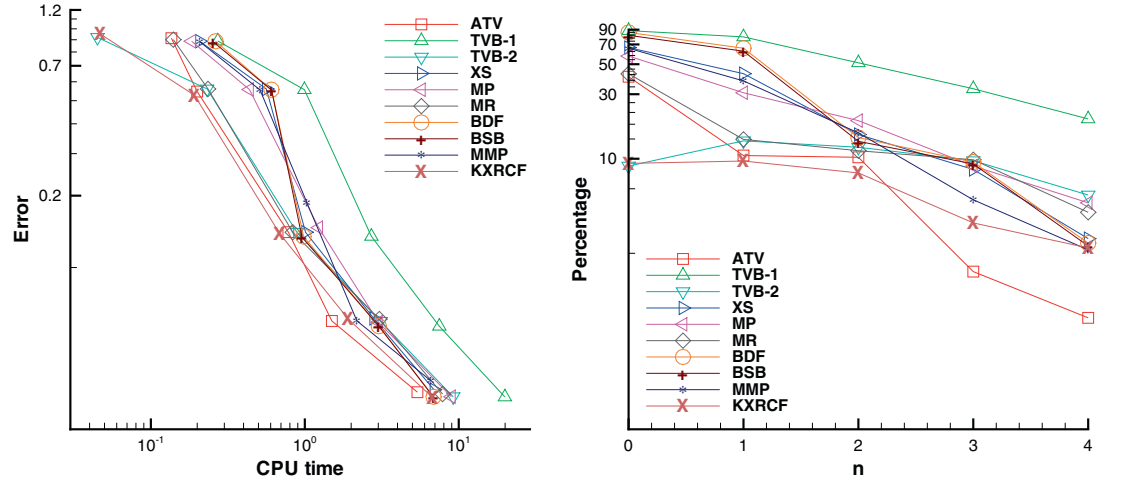

Fig. 3.8. The shock density wave interaction problem by the 7th-order scheme. CPU-L_1-error (left) and cell-percentage (right).

When $\phi \neq 1$, the limiter enacts, the cell I_j is identified as a troubled cell.

9. A shock-detection technique by Krivodonova et al. [15] (KXRCF). Partition the boundary of a cell I_j into two portions ∂I_j^- and ∂I_j^+, where the flow is into ($\vec{v}\cdot\vec{n} < 0, \vec{n}$ is the normal vector to ∂I_j) and out of ($\vec{v}\cdot\vec{n} > 0$)I_j, respectively. The cell I_j is identified as a troubled cell, if:

$$\frac{\left|\int_{\partial I_j^-}(u^h|_{I_j} - u^h|_{I_{n_j}})ds\right|}{h_j^{\frac{k+1}{2}}\left|\partial I_j^-\right|\|u^h|_{I_j}\|} > 1, \tag{2.21}$$

here h_j is the radius of the circumscribed circle in the element I_j. I_{n_j} is the neighbor of I_j on the side of ∂I_j^- and the norm is based on an element average in one-dimensional case.

Remark 2. From the above list of the indicators, we observe that ATV, TVB, XS, MP and MR indicators are dependent on parameters, while the remaining indicators, i.e., BDF, BSB, MMP and KXRCF indicators are free of parameters. The parameter-free indicator is desirable for general hyperbolic conservation laws. We use the solution u itself as indicator variable for the one-dimensional scalar problems. For system of equations of gas dynamics, i.e., the one- and two-dimensional Euler equations are considered, we use the entropy as indicator variable. For the two-dimensional Euler equations, the troubled-cell indicators work in x- and y-direction, respectively, to identify the troubled cells.

Remark 3. For the indicators except ATV are depended only the cell and its two neighbor cells and the reconstruction of numerical flux is depended on the cell and its $2r$ neighbor cells, these local properties guarantee that this hybrid approach is a high parallel method.

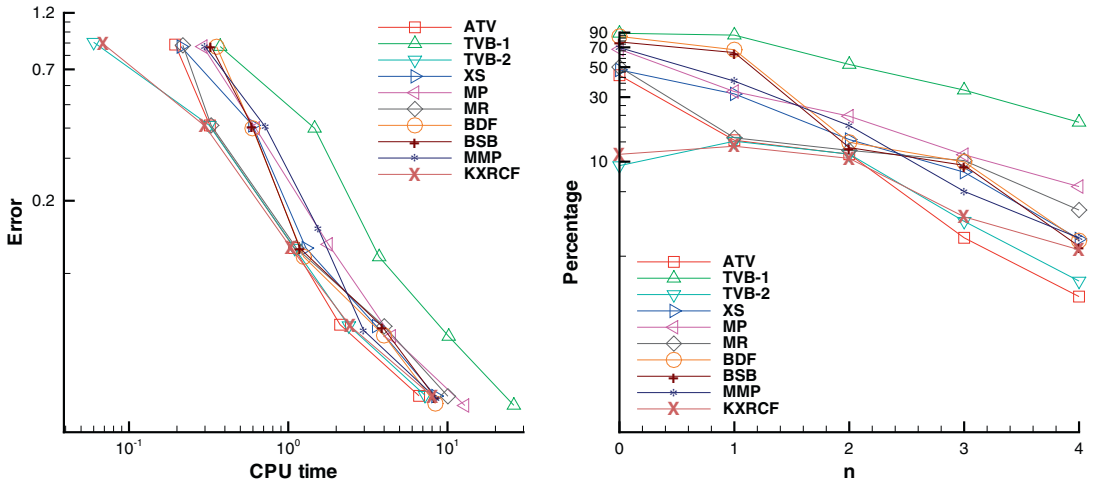

Fig. 3.9. The shock density wave interaction problem by the 9th-order scheme. CPU-L_1-error (left) and cell-percentage (right).

Table 3.3
Shock density wave interaction problem. The total CPU time of $N = 100 \times 2^n$ ($n = 0,1,\ldots,4$) cells, and the ratios of the total CPU time by the 3rd, 5th, 7th and 9th-order hybrid WENO schemes over that of the same order pure WENO scheme.

Scheme or indicators	Third-order scheme		Fifth-order scheme		Seventh-order scheme		Ninth-order scheme	
	CPU	Ratio	CPU	Ratio	CPU	Ratio	CPU	Ratio
WENO	19.16309	1.00	37.69527	1.00	99.80983	1.00	142.95627	1.00
ATV	4.01739	0.21	4.99924	0.13	7.75382	0.08	10.35942	0.07
TVB-1	6.62199	0.35	12.25314	0.33	27.02989	0.27	41.94762	0.29
TVB-2	4.45732	0.23	5.61315	0.15	12.67507	0.13	11.12931	0.08
XS	4.40133	0.23	6.26605	0.17	11.01133	0.11	14.15385	0.10
MP	5.09523	0.27	6.34004	0.17	12.35912	0.12	20.01796	0.14
MR	4.42233	0.23	6.48601	0.17	11.58724	0.12	15.88159	0.11
BDF	4.33534	0.23	6.40003	0.17	11.04232	0.11	15.27768	0.11
BSB	4.49732	0.23	6.69298	0.18	11.04132	0.11	14.81975	0.10
MMP	4.86926	0.25	6.06808	0.16	9.89050	0.10	14.06386	0.10
KXRCF	4.49132	0.23	5.63314	0.15	9.17560	0.09	11.97018	0.08

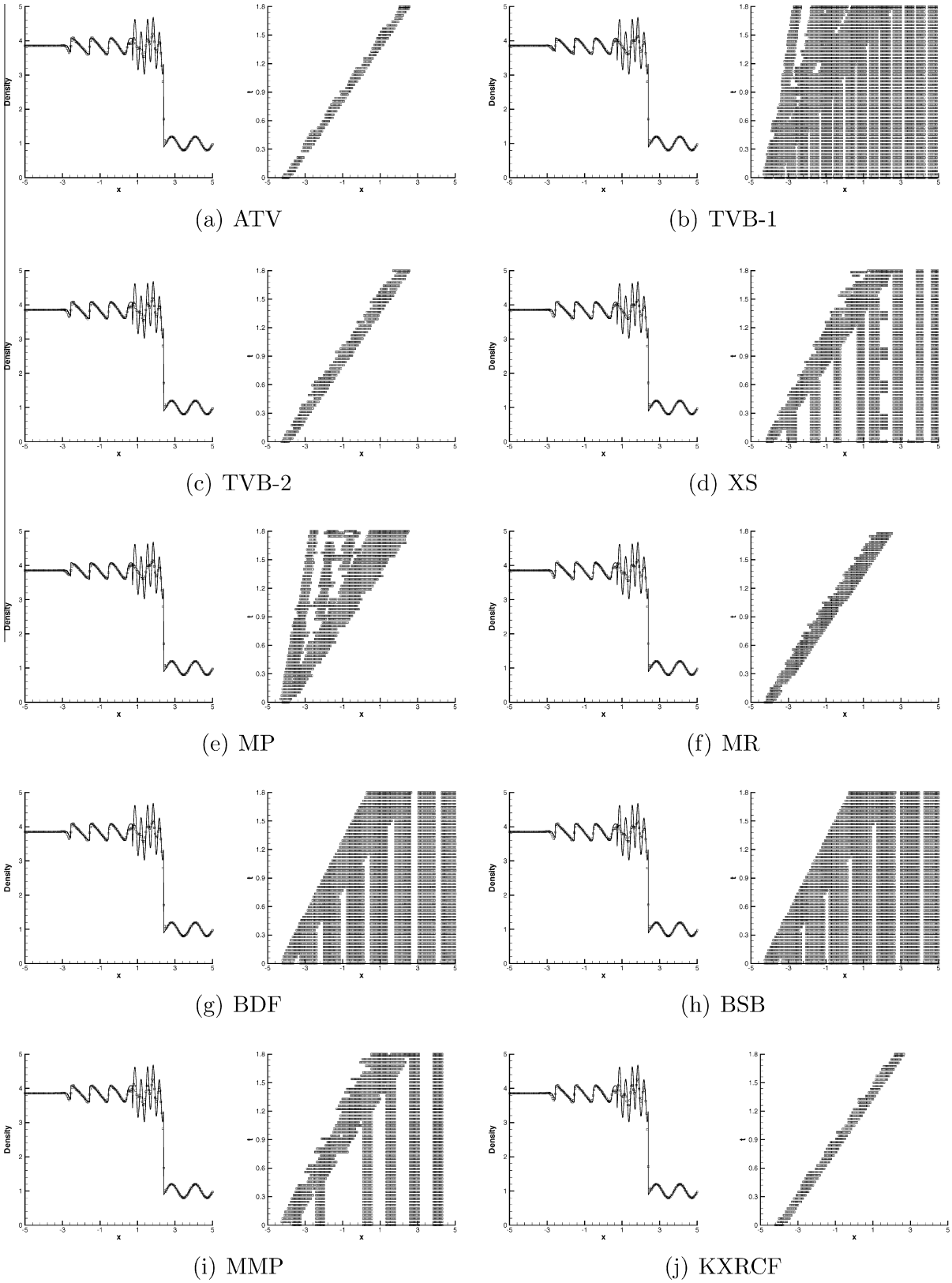

Fig. 3.10. Shock density wave interaction problem by the 5th-order scheme with different indicators, 200 cells, $t = 1.8$. Density and time history of reconstruction of fluxes by WENO approximation.

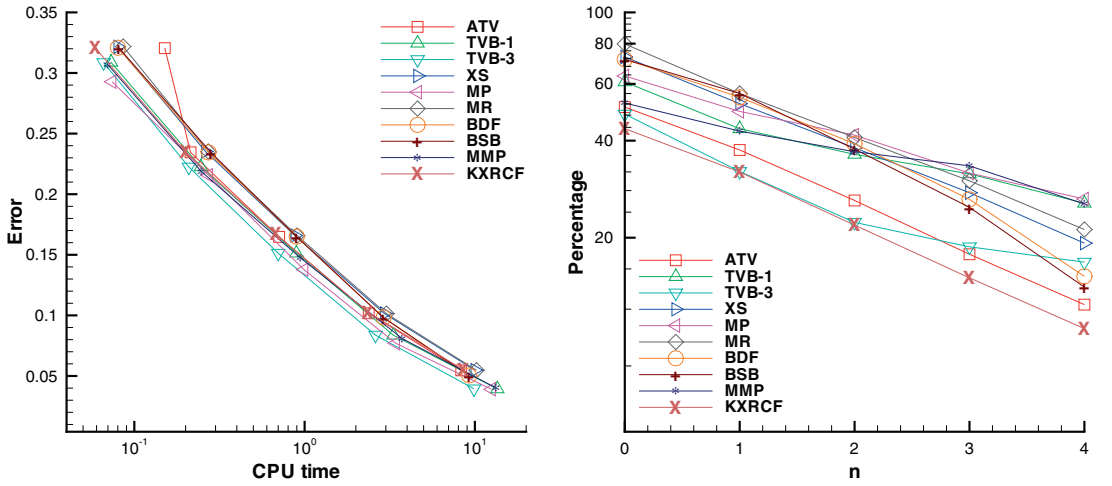

Fig. 3.11. The blast wave problem by the 3rd-order scheme. CPU-L_1-error (left) and cell-percentage (right).

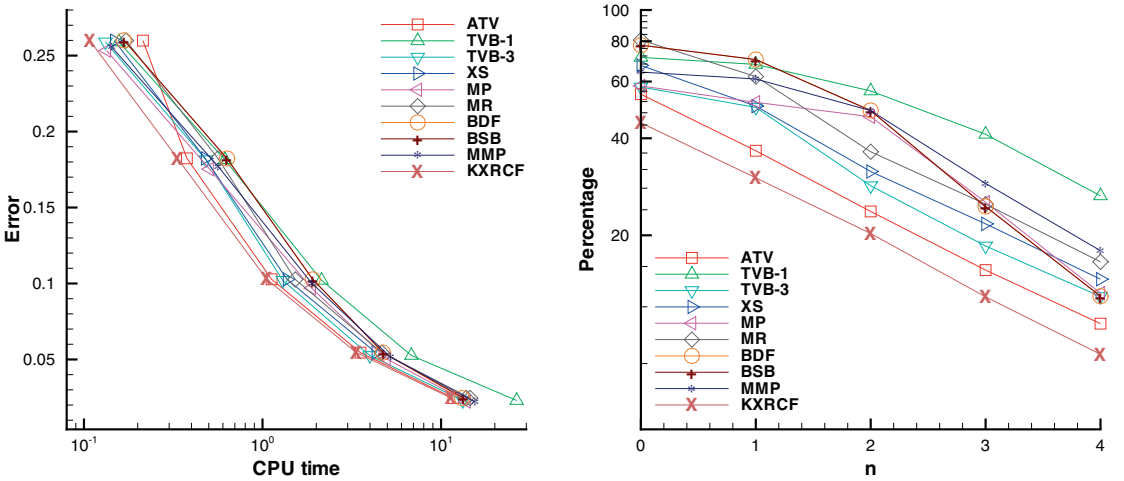

Fig. 3.12. The blast wave problem by the 5th-order scheme. CPU-L_1-error (left) and cell-percentage (right).

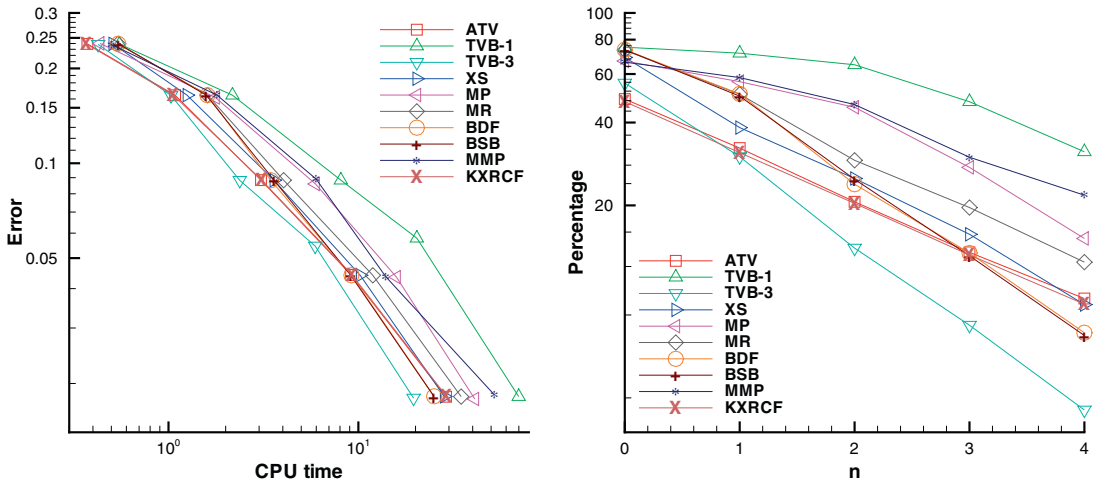

Fig. 3.13. The blast wave problem by the 7th-order scheme. CPU-L_1-error (left) and cell-percentage (right).

3. Numerical results

In this section we perform extensive numerical experiments on one- and two-dimensional Euler equations to compare the performances of hybrid WENO schemes using the troubled-cell indicators outlined in the previous section. Comparisons are concentrated mainly on the CPU time, the L_1-error, and the percentage of reconstruction of fluxes by WENO approximation. For the blast wave problem, the ATV parameter θ is taken as 0.1; for other problems it is taken θ as 0.7. The notations TVB-1, TVB-2 and TVB-3 refer to the minmod-based TVB indicator with the TVB parameters $M = 0.01$, $M = 10$ and $M = 100$, respectively. The multi-resolution parameter ε_{MR} is taken as 0.25 for the blast wave problem, and 0.5 for the remaining problems. In all the numerical tests of this paper, the third order Runge–Kutta method is used for time discretization, and the CFL number is taken as 0.6.

3.1. One-dimensional case

In this subsection, we consider the one-dimensional Euler equations of gas dynamics with three different initial conditions. The PDEs are

$$\begin{bmatrix} \rho \\ \rho v \\ E \end{bmatrix}_t + \begin{bmatrix} \rho v \\ \rho v^2 + p \\ v(E+p) \end{bmatrix}_x = 0,$$

here ρ is the density, v is the velocity, E is the total energy, p is the pressure, which is related to the total energy by $E = \frac{p}{\gamma-1} + \frac{1}{2}\rho v^2$ with $\gamma = 1.4$.

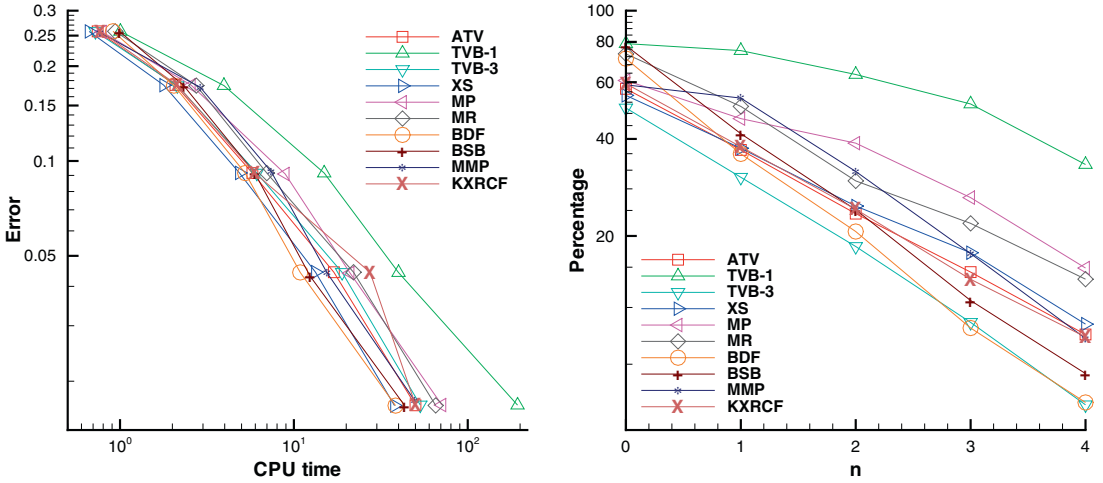

Fig. 3.14. The blast wave problem by the 9th-order scheme. CPU-L_1-error (left) and cell-percentage (right).

Table 3.4
Blast wave problem. The total CPU time of $N = 100 \times 2^n$ ($n = 0,1,\ldots,4$) cells, and the ratios of the total CPU time by the 3rd, 5th, 7th and 9th order hybrid WENO schemes over that of the same order pure WENO scheme.

Scheme or indicators	Third-order scheme		Fifth-order scheme		Seventh-order scheme		Ninth-order scheme	
	CPU	Ratio	CPU	Ratio	CPU	Ratio	CPU	Ratio
WENO	36.96038	1.00	72.70895	1.00	265.38466	1.00	453.34208	1.00
ATV	11.55224	0.31	16.81544	0.23	43.38540	0.16	76.12243	0.17
TVB-1	18.07225	0.47	36.31648	0.50	103.73023	0.39	253.44817	0.56
TVB-3	13.37497	0.36	19.18508	0.26	29.62150	0.11	81.78057	0.18
XS	14.20984	0.38	20.26292	0.28	44.72219	0.17	58.79406	0.13
MP	17.24138	0.47	21.40975	0.29	66.47590	0.25	105.09502	0.23
MR	14.49980	0.39	18.36121	0.25	54.03979	0.20	73.18987	0.16
BDF	13.33597	0.36	20.53588	0.28	40.61683	0.15	57.86320	0.13
BSB	13.33297	0.36	20.84783	0.29	40.54884	0.15	65.44105	0.14
MMP	18.32022	0.50	23.36245	0.32	76.09943	0.28	76.58036	0.17
KXRCF	11.81121	0.32	16.20354	0.22	43.70336	0.16	86.93278	0.19

Example 4.1. The Lax problem. The initial condition is

$$(\rho, v, p) = \begin{cases} (0.445, 0.698, 3.528) & \text{if } x \leqslant 0, \\ (0.5, 0, 0.571) & \text{if } x > 0. \end{cases}$$

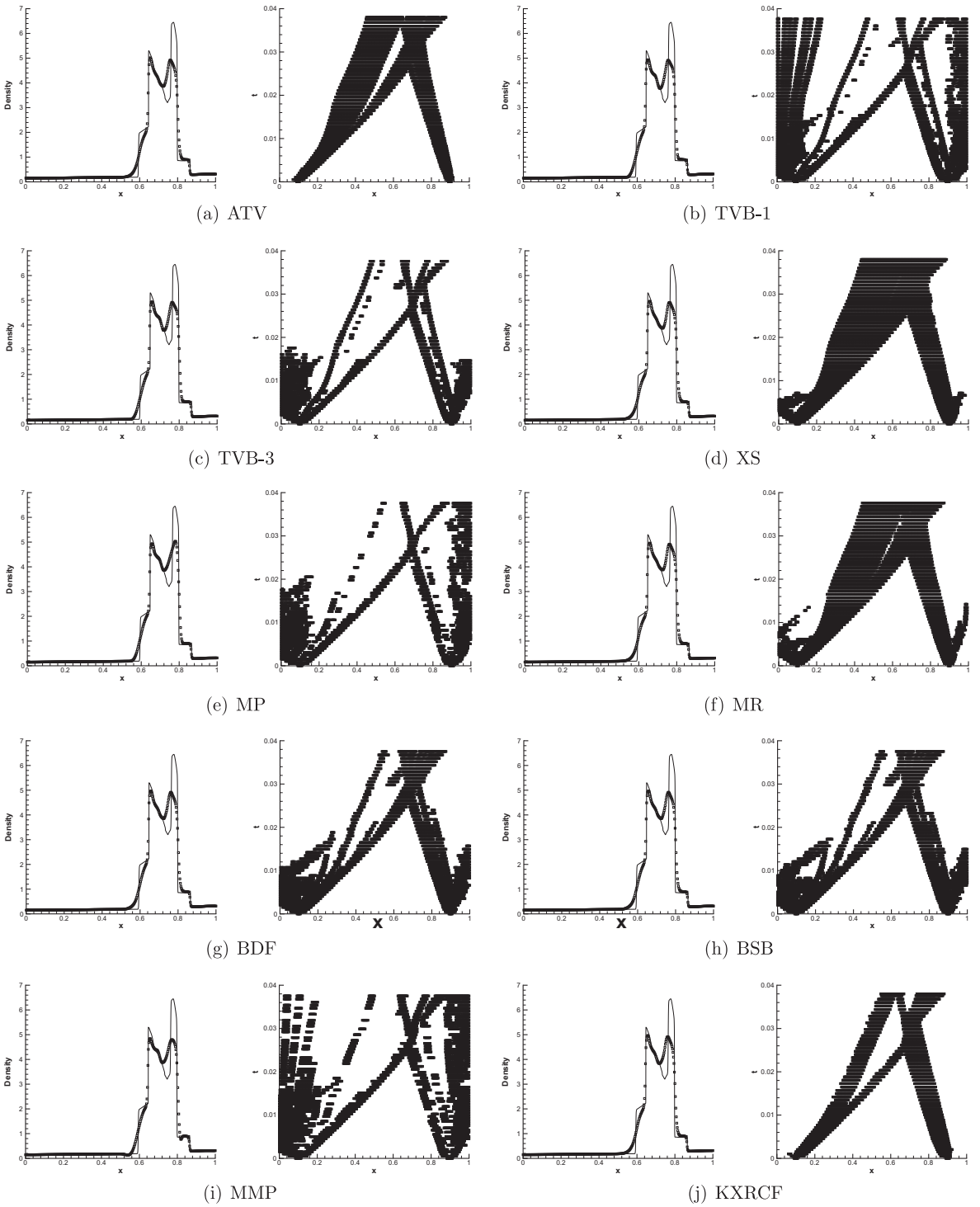

Fig. 3.15. Blast wave problem by the 3rd-order scheme with different indicators, 400 cells, $t = 0.038$. Density and time history of reconstruction of fluxes by WENO approximation.

The computational domain is $[-5,5]$, and we compute this problem till $t = 1.3$.

We first compare the performances of hybrid WENO schemes with different troubled-cell indicators. We compute the L_1-error of density, CPU time and the percentage of reconstruction of fluxes by WENO approximation of all indicators using

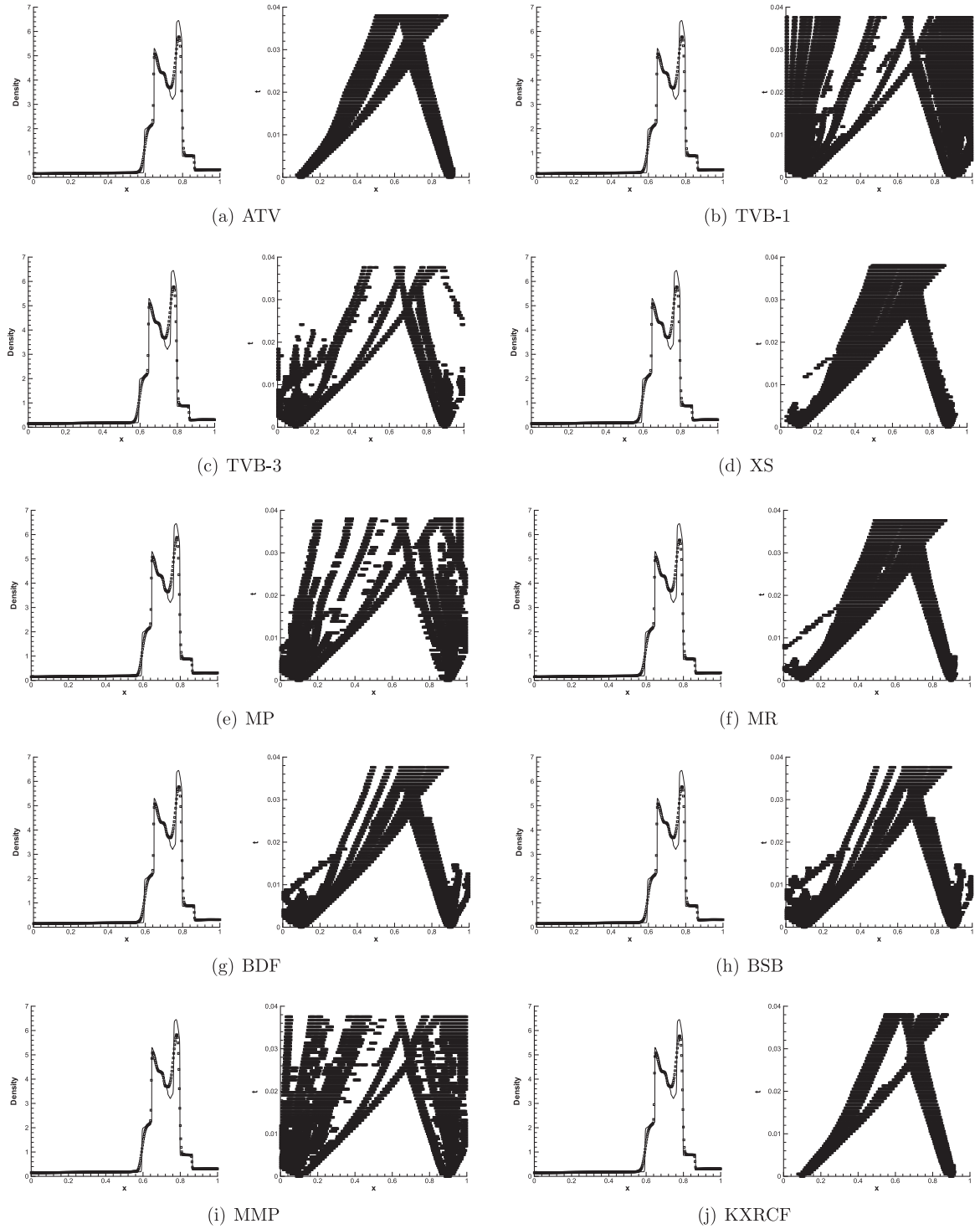

Fig. 3.16. Blast wave problem by the 5th-order scheme with different indicators, 400 cells, $t = 0.038$. Density and time history of reconstruction of fluxes by WENO approximation.

100×2^n ($n = 0,\ldots,4$) uniform cells and show CPU-L_1-error curves and cell-percentage curves in Figs. 3.1–3.4. CPU time comparison among pure and hybrid WENO schemes is given in Table 3.2.

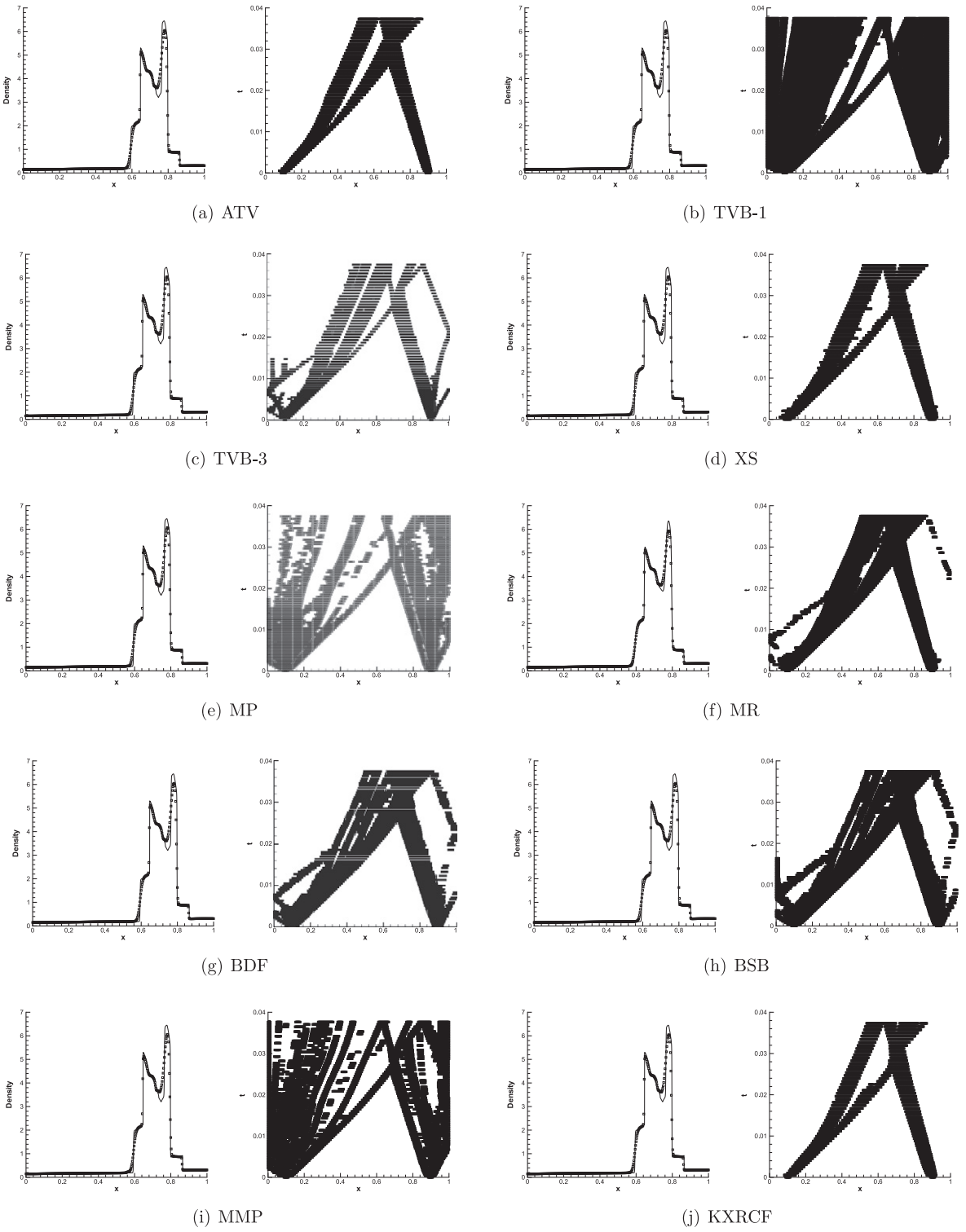

Fig. 3.17. Blast wave problem by the 7th-order scheme with different indicators, 400 cells, $t = 0.038$. Density and time history of reconstruction of fluxes by WENO approximation.

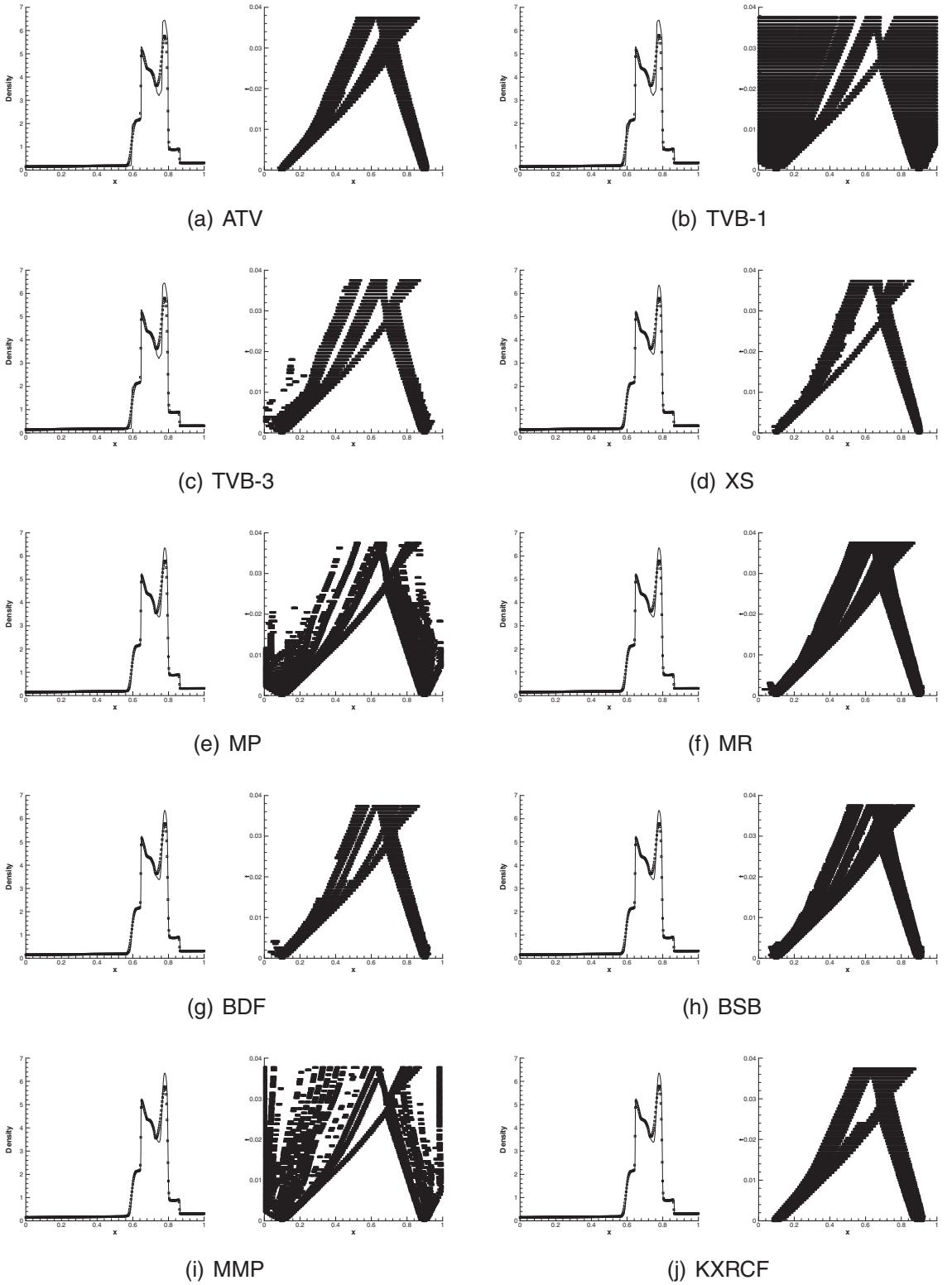

Fig. 3.18. Blast wave problem by the 9th-order scheme with different indicators, 400 cells, $t = 0.038$. Density and time history of reconstruction of fluxes by WENO approximation.

All comparisons above suggest that for Lax problem, the winners in terms of less CPU time, smaller percentage of reconstruction of fluxes by WENO approximation and more accurate numerical solutions, are ATV, TVB-2, MR and KXRCF indicators. We can observe that the percentages of reconstruction of fluxes by WENO approximation decrease with mesh refinement in almost cases, which is a very desirable property for troubled-cell indicators. Hybrid WENO schemes can save more CPU time than pure WENO schemes, and this property is more obvious with mesh refinement.

For all the indicators, we show the computed density ρ at $t = 1.3$ against the exact solution and time history of reconstruction of fluxes by WENO approximation with $N = 200$ uniform cells in Fig. 3.5 by the 5th-order scheme. In the density figure, the solid line is the exact solution and "□" represents the numerical solution. In the time history figure, each "□" represents the reconstruction of flux by WENO approximation. We can also observe that the numerical results for all cases keep sharp transition and are mostly oscillation-free. In order to save space, in this paper we do not show the results by the 3rd-, 7th- and 9th-order schemes which are similar to those by the 5th-order scheme.

Example 4.2. The shock density wave interaction problem. The solution of this problem contains both shocks and complex smooth regions. The initial condition is

$$(\rho, v, p) = \begin{cases} (3.857143, 2.629369, 10.333333) & \text{if } x < -4, \\ (1 + 0.2\sin(5x), 0, 1) & \text{if } x \geqslant -4. \end{cases}$$

The computational domain is $[-5,5]$, and we compute this problem till $t = 1.8$.

Again we show CPU-L_1-error and cell-percentage curves of all indicators using 100×2^n ($n = 0,\ldots,4$) uniform cells in Figs. 3.6–3.9. CPU time comparison among pure and hybrid WENO schemes for this problem is given in Table 3.3.

Table 3.3 suggests that hybrid WENO schemes can save more CPU time than pure WENO schemes. From Figs. 3.6–3.9 and Table 3.3, we observe that for the shock density wave interaction problem, ATV, TVB-2, MR and KXRCF indicators are better than others, for they result in less CPU time, smaller percentages of reconstruction of fluxes by WENO approximation and more accurate numerical solutions.

For all the indicators, we present the computed density ρ against the reference "exact" solution and time history of reconstruction of fluxes by WENO approximation with 200 uniform cells in Fig. 3.10 by the 5th-order scheme. The reference "exact" solution is computed by the 5th-order finite difference WENO scheme [14] with 6400 grid points. Again, in order to save space, in this paper we do not show the results by the 3rd-, 7th- and 9th-order methods which are similar to those by the 5th-order scheme.

Example 4.3. The blast wave problem. This problem involves interaction of blast waves and its initial condition is given by

$$(\rho, v, p) = \begin{cases} (1, 0, 1000) & \text{if } 0 \leqslant x < 0.1, \\ (1, 0, 0.01) & \text{if } 0.1 \leqslant x < 0.9, \\ (1, 0, 100) & \text{if } 0.9 \leqslant x \leqslant 1. \end{cases}$$

A reflective boundary condition is applied at both ends, see [11,26] for details. The computational domain is $[0,1]$, and we compute the solution up to $t = 0.038$.

Analogously we show CPU-L_1-error and cell-percentage curves of all indicators using 100×2^n ($n = 0,\ldots,4$) uniform cells in Figs. 3.11–3.14. We present the comparison on CPU time among pure and hybrid WENO schemes in Table 3.4.

Table 3.5
Double mach reflection problem. Comparison on CPU time and percentage of reconstruction of fluxes by WENO approximation among pure WENO and hybrid WENO schemes.

$N_x \times N_y$	Scheme or indicators	Third-order scheme		Fifth-order scheme	
		CPU	Percent	CPU	Percent
480×120	WENO	529.05	100.00	723.59	100.00
	ATV	118.43	8.59	129.53	9.96
	TVB-3	103.30	4.80	127.77	7.47
	MR	103.58	7.99	124.92	8.42
	KXRCF	114.24	5.31	145.54	6.33
960×240	WENO	5928.03	100.00	9374.70	100.00
	ATV	1145.37	6.99	1433.27	7.44
	TVB-3	1050.23	3.55	1379.08	5.96
	MR	1064.82	5.38	1256.15	5.78
	KXRCF	1312.24	3.61	1505.23	4.39
1920×480	WENO	40262.41	100.00	62511.25	100.00
	ATV	10530.14	5.61	11384.43	6.03
	TVB-3	8150.48	2.72	11048.70	5.29
	MR	7759.46	3.56	9536.02	3.88
	KXRCF	8817.95	2.30	11257.59	3.24

Figs. 3.11–3.14 and Table 3.4 indicate that for the blast wave problem, ATV, TVB-3 and KXRCF indicators are better than other indicators, for they are more efficient and more accurate than others. Table 3.4 suggests that hybrid WENO schemes is more efficient than pure WENO schemes.

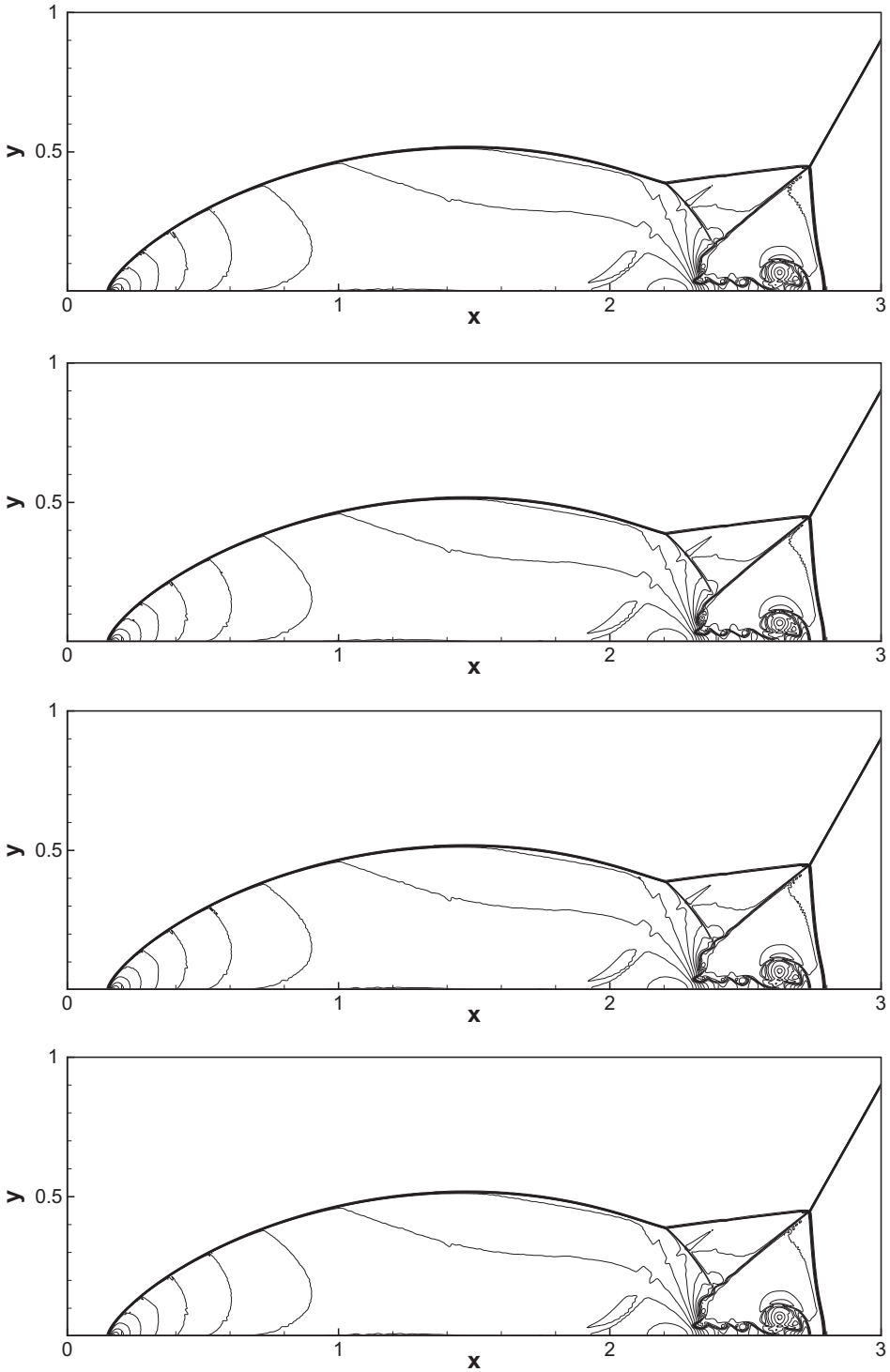

Fig. 3.19. Double Mach reflection problem by the 5th-order scheme with 1920 × 480 cells, $t = 0.2$. Thirty equally spaced density contours from 1.5 to 22.7. From top to bottom: ATV, TVB-3, MR and KXRCF.

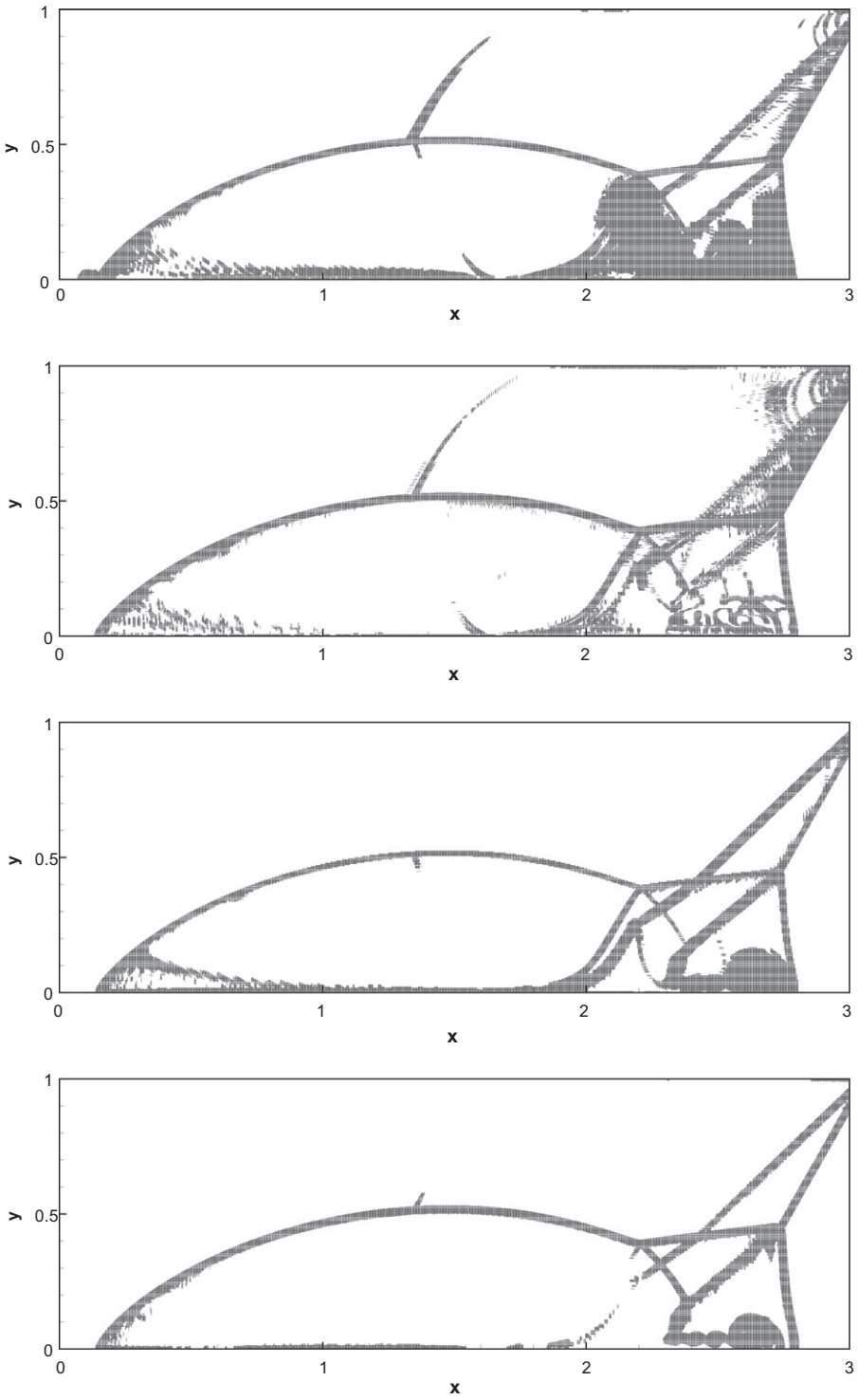

Fig. 3.20. Double Mach reflection problem by the 5th-order scheme with 1920×480 cells, $t = 0.2$. Reconstructions of fluxes by WENO approximation at the last time step. From top to bottom: ATV, TVB-3, MR and KXRCF.

In Figs. 3.15–3.18, we present the computed density ρ and time history of reconstruction of fluxes by WENO approximation with all the indicators with 400 uniform cells by the 3rd-, 5th-, 7th- and 9th-order schemes. The reference "exact" solution is also computed by the 5th-order finite difference WENO scheme [14] using 6400 grid points.

3.2. Two-dimensional case

In the one-dimensional cases, the performances of ATV, TVB (when the TVB parameter M is chosen suitably), MR and KXRCF indicators are better than others. Now, we consider hybrid WENO schemes with the above indicators for the two-dimensional Euler equations of gas dynamics with two different initial conditions. The PDEs are

$$\begin{bmatrix} \rho \\ \rho u \\ \rho v \\ E \end{bmatrix}_t + \begin{bmatrix} \rho u \\ \rho u^2 + p \\ \rho uv \\ u(E+p) \end{bmatrix}_x + \begin{bmatrix} \rho v \\ \rho uv \\ \rho v^2 + p \\ v(E+p) \end{bmatrix}_y = 0,$$

here ρ is the density, (u, v) is the velocity, E is the total energy, p is the pressure, which is related to the total energy by $E = \frac{p}{\gamma-1} + \frac{1}{2}\rho(u^2 + v^2)$ with $\gamma = 1.4$.

Example 4.4. Double Mach reflection. This problem is originally from [26]. The computational domain for this problem is $[0,4] \times [0,1]$. The reflecting wall lies at the bottom, starting from $x = \frac{1}{6}$. Initially a right-moving Mach 10 shock is positioned at $x = \frac{1}{6}, y = 0$ and makes a 60° angle with the x-axis. For the bottom boundary, the exact post-shock condition is imposed for the part from $x = 0$ to $x = \frac{1}{6}$ and a reflective boundary condition is used for the rest. At the top boundary, the flow values are set to describe the exact motion of a Mach 10 shock. We compute the solution up to $t = 0.2$.

In Table 3.5 we document the CPU time and the percentages of reconstruction of fluxes by WENO approximation by the 3rd- and 5th-order schemes with the ATV, TVB-3, MR and KXRCF indicators. We can see that the hybrid WENO schemes cost about one fifth and one sixth CPU time of pure WENO scheme for the 3rd-order and the 5th-order schemes, respectively. We also see that the percentages of reconstruction of fluxes by WENO approximation for hybrid WENO methods is less than 10 for both by the 3rd- and the 5th-order schemes with the TVB-3, MR and KXRCF indicators, and the smaller percentage of reconstruction of fluxes by WENO approximation with the finer meshes as we expect. To save space, we only show the numerical results on the most refined mesh with 1920×480 uniform cells by the 5th-order scheme with ATV, TVB-3, MR and KXRCF indicators in Fig. 3.19. All the figures are showing 30 equally spaced density contours from 1.5 to 22.7. Reconstructions of fluxes by WENO approximation at the last time step with the ATV, TVB-3, MR and KXRCF indicators are shown in Fig. 3.20.

Example 4.5. A Mach 3 wind tunnel with a step. This model problem is also originally from [26]. The setup of the problem is as follows. The wind tunnel is 1 length unit wide and 3 length units long. The step is 0.2 length units high and is located 0.6 length units from the left-hand end of the tunnel. The problem is initialized by a right-going Mach 3 flow. Reflective boundary conditions are applied along the wall of the tunnel and in/out flow boundary conditions are applied at the entrance/exit. The corner of the step is a singular point and we treat it the same way as in [26], which is based on the assumption of a nearly steady flow in the region near the corner. We compute the solution up to $t = 4$.

In Table 3.6 we document the CPU time and the percentages of reconstruction of fluxes by WENO approximation by the 3rd- and the 5th-order schemes with the ATV, TVB-3, MR and KXRCFR indicators. We again can see that the hybrid WENO schemes cost about one third and one fourth (except KXRCF, which is about one third) CPU time of pure WENO scheme for

Table 3.6
Forward step problem. Comparison on CPU time and percentage of reconstruction of fluxes by WENO approximation among pure WENO and hybrid WENO schemes.

$N_x \times N_y$	Scheme or indicators	Third-order scheme		Fifth-order scheme	
		CPU	Percent	CPU	Percent
240×80	WENO	304.27	100.00	422.07	100.00
	ATV	159.21	20.63	178.97	21.10
	TVB-3	111.90	8.01	149.92	10.35
	MR	122.26	16.46	136.45	13.72
	KXRCF	147.74	18.27	182.11	19.90
480×160	WENO	2708.42	100.00	3437.47	100.00
	ATV	907.25	11.36	1228.32	12.05
	TVB-3	926.42	6.60	1070.11	7.76
	MR	891.61	11.05	998.60	9.79
	KXRCF	1040.93	13.15	1234.79	13.95
960×320	WENO	22960.60	100.00	29965.77	100.00
	ATV	7497.02	5.81	7816.95	6.54
	TVB-3	7989.90	4.46	8356.79	6.53
	MR	7098.19	6.51	7689.53	6.33
	KXRCF	7579.88	8.58	9172.84	9.87

the 3rd-order and the 5th-order schemes, respectively. We also see that the percentage of numerical fluxes using the WENO approximation for hybrid WENO methods is less than 20 for both by the 3rd- and the 5th-order schemes with the ATV, TVB-3, MR and KXRCF indicators, and the smaller percentage of reconstruction of fluxes by WENO approximation with the finer meshes as we expect. To save space, we only show the numerical results on the most refined mesh with 960 × 320 uniform

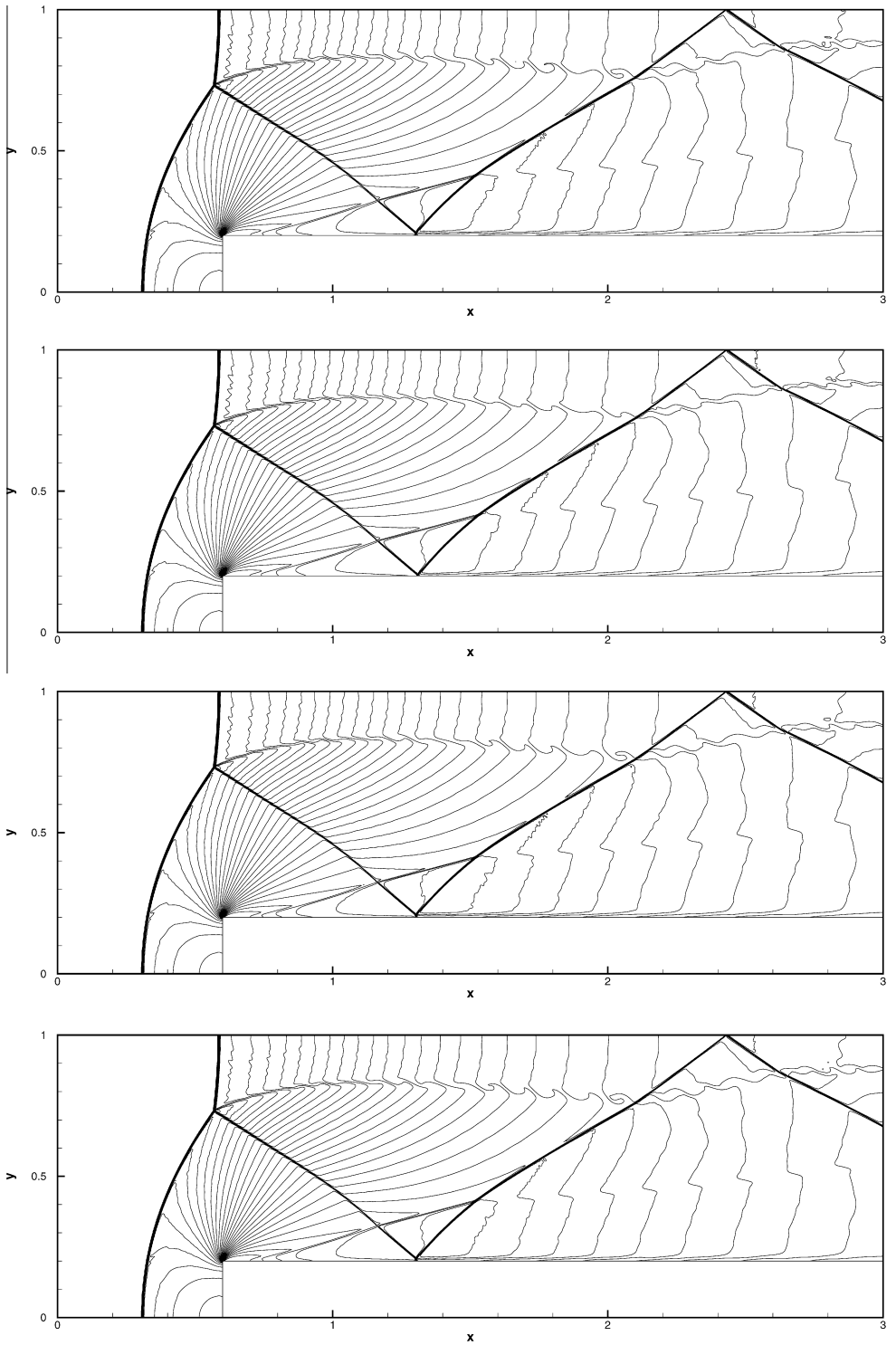

Fig. 3.21. Forward step problem by the 5th-order scheme with 960 × 320 cells, $t = 4$. Thirty equally spaced density contours from 0.32 to 6.15. From top to bottom: ATV, TVB-3, MR and KXRCF.

cells by the 5th-order scheme with the ATV, TVB-3, MR and KXRCF indicators in Fig. 3.21. All the figures are showing 30 equally spaced density contours form 0.32 to 6.15. Reconstructions of fluxes by WENO approximation at the last time step with the ATV, TVB-3, MR and KXRCF indicators are shown in Fig. 3.22.

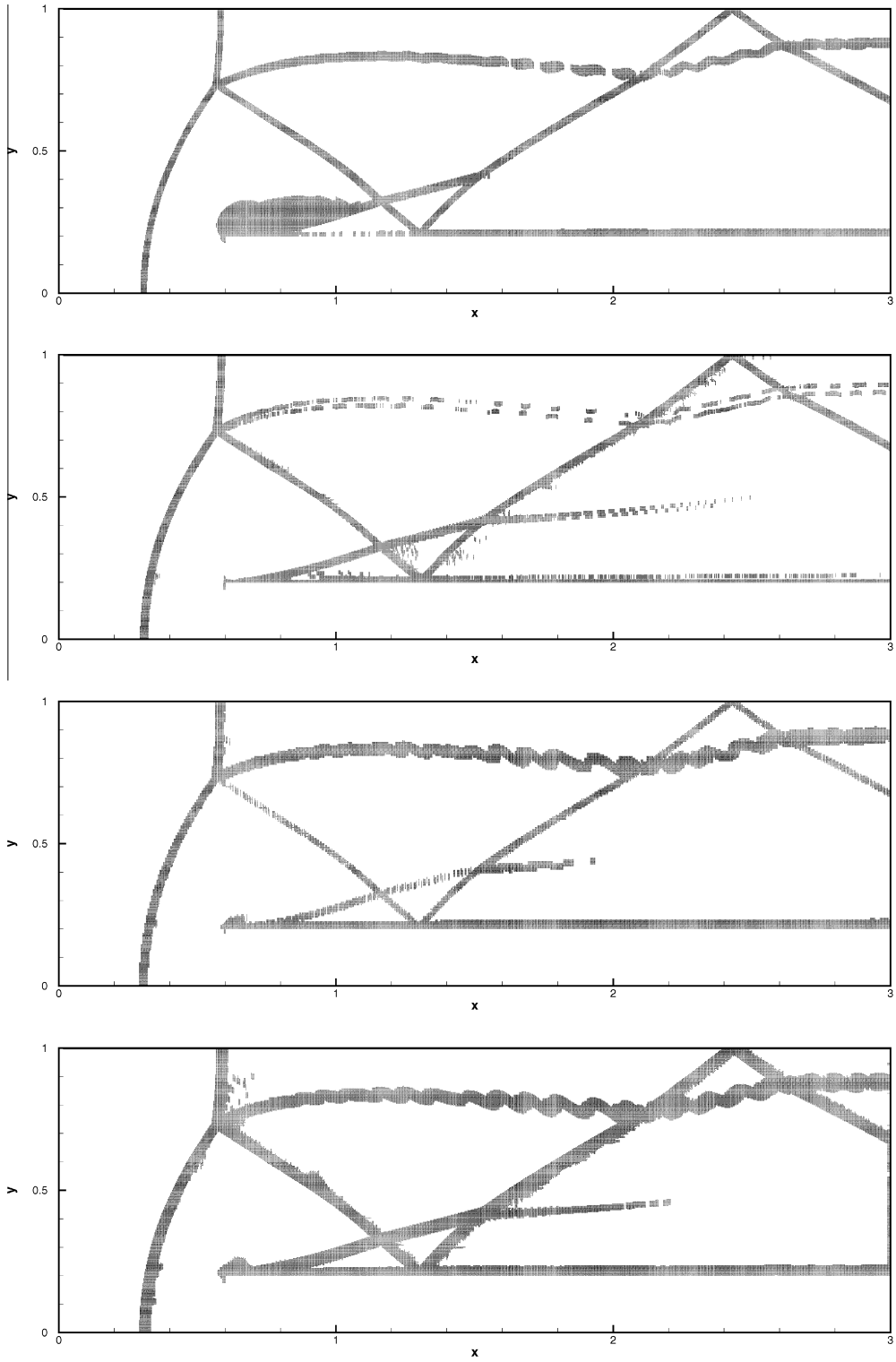

Fig. 3.22. Forward step problem by the 5th-order scheme with 960 × 320 cells, $t = 4$. Reconstructions of fluxes by WENO approximation at the last time step. From top to bottom: ATV, TVB-3, MR and KXRCF.

4. Concluding remarks

In this paper, we have systematically investigated and compared a few different troubled-cell indicators for the hybrid WENO finite difference schemes. Extensive one-dimensional simulations on the hyperbolic systems of Euler equations indicate that the ATV, TVB (when the TVB parameter M is chosen suitably), MR and KXRCF indicators are better than other indicators. We also apply hybrid WENO schemes with these "best" indicators for the two-dimensional Euler equations, the numerical results again indicate that hybrid WENO schemes are more efficient than WENO schemes. The hybrid WENO scheme with these "best" indicators is efficient and reliable, which saves computational cost and obtain non spurious oscillatory numerical solutions. This approach can also be applied to the hybrid WENO finite volume schemes, and the research on the hybrid WENO finite volume schemes with indicators and the implementation of the method for structured curved meshes and three-dimensional problems are ongoing.

References

[1] R. Biswas, K. Devine, J. Flaherty, Parallel, adaptive finite element methods for conservation laws, Applied Numerical Mathematics 14 (1994) 255–283.
[2] D.S. Balsara, C.-W. Shu, Monotonicity preserving WENO schemes with increasingly high-order of accuracy, Journal of Computational Physics 160 (2000) 405–452.
[3] A. Burbeau, P. Sagaut, C.H. Bruneau, A problem-independent limiter for high-order Runge–Kutta discontinuous Galerkin methods, Journal of Computational Physics 169 (2001) 111–150.
[4] B. Cockburn, S. Hou, C.-W. Shu, The Runge–Kutta local projection discontinuous Galerkin finite element method for conservation laws IV: the multidimensional case, Mathematics of Computation 54 (1990) 545–581.
[5] B. Cockburn, S.-Y. Lin, C.-W. Shu, TVB Runge–Kutta local projection discontinuous Galerkin finite element for conservation laws III: one dimensional systems, Journal of Computational Physics 84 (1989) 90–113.
[6] B. Cockburn, C.-W. Shu, TVB Runge–Kutta local projection discontinuous Galerkin finite element method for conservation laws II: general framework, Mathematics of Computation 52 (1989) 411–435.
[7] B. Cockburn, C.-W. Shu, The Runge–Kutta discontinuous Galerkin finite element method for conservation laws V: multidimensional systems, Journal of Computational Physics 141 (1998) 199–224.
[8] T. Colonius, S.K. Lele, Computational aeroacoustics: progress on nonlinear problems of soundgeneration, Progress in Aerospace Sciences 40 (2004) 345–416.
[9] B. Cosat, W.S. Don, High order hybrid central-WENO finite difference scheme for conservation laws, Journal of Computational and Applied Mathematics 204 (2007) 209–218.
[10] G.A. Gerolymos, D. Sénéchal, I. Vallet, Very-high-order WENO schemes, Journal of Computational Physics 228 (2009) 8481–8524.
[11] A. Harten, B. Engquist, S. Osher, S.R. Chakravarthy, Uniformly high order accurate essentially non-oscillatory, schemes: III, Journal of Computational Physics 71 (1987) 231–303.
[12] A. Harten, Adaptive multiresolution schemes for shock computations, Journal of Computational Physics 115 (1994) 319–338.
[13] D.J. Hill, D.I. Pullin, Hybrid tuned center-difference-WENO method for large eddy simulations in the presence of strong shocks, Journal of Computational Physics 194 (2004) 435–450.
[14] G. Jiang, C.-W. Shu, Efficient implementation of weighted ENO schemes, Journal of Computational Physics 126 (1996) 202–228.
[15] L. Krivodonova, J. Xin, J.-F. Remacle, N. Chevaugeon, J. Flaherty, Shock detection and limiting with discontinuous Galerkin methods for hyperbolic conservation laws, Applied Numerical Mathematics 48 (2004) 323–338.
[16] X.D. Liu, S. Osher, T. Chan, Weighted essentially non-oscillatory schemes, Journal of Computational Physics 115 (1994) 200–212.
[17] S. Pirozzoli, Conservative hybrid compact-WENO schemes for shock-turbulence interaction, Journal of Computational Physics 178 (2002) 81–117.
[18] J. Qiu, C.-W. Shu, A comparison of troubled-cell indicators for Runge–Kutta discontinuous Galerkin methods using weighted essentially nonoscillatory limiters, SIAM Journal of Scientific Computing 27 (2005) 995–1013.
[19] W.J. Rider, L.G. Margolin, Simple modifications of monotonicity-preserving limiters, Journal of Computational Physics 174 (2001) 473–488.
[20] C.-W. Shu, S. Osher, Efficient implementation of essentially non-oscillatory shock-capturing schemes, Journal of Computational Physics 77 (1988) 439–471.
[21] C.-W. Shu, S. Osher, Efficient implementation of essentially non-oscillatory shock-capturing schemes, II, Journal of Computational Physics 83 (1989) 32–78.
[22] C.-W. Shu, Essentially non-oscillatory and weighted essentially non-oscillatory schemes for hyperbolic conservation laws, NASA/CR-97-206253, ICASE Report No. 97-65.
[23] C.-W. Shu, High order weighted essentially nonoscillatory schemes for convection dominated problems, SIAM Review 51 (2009) 82–126.
[24] A. Suresh, H.T. Huynh, Accurate monotonicity-preserving schemes with Runge–Kutta time stepping, Journal of Computational Physics 136 (1997) 83–99.
[25] E.M. Taylor, M. Wu, M.P. Martn, Optimization of nonlinear error for weighted essentially non-oscillatory methods in direct numerical simulations of compressible turbulence, Journal of Computational Physics 223 (2007) 384–397.
[26] P. Woodward, P. Colella, The numerical simulation of two-dimensional fluid flow with strong shocks, Journal of Computational Physics 54 (1984) 115–173.
[27] Z. Xu, C.-W. Shu, Anti-diffusive flux corrections for high order finite difference WENO schemes, Journal of Computational Physics 205 (2005) 458–485.
[28] H. Zhu, J. Qiu, Adaptive Runge–Kutta discontinuous Galerkin methods using different indicators: one-dimensional case, Journal of Computational Physics 228 (2009) 6957–6976.